2005

Deep-UV Light Emitting Diodes: An Experimental Investigation of Characterization and Optimization Techniques

Eric M. Fraser
Pomona College

Deep-UV Light Emitting Diodes:

An Experimental Investigation of Characterization and Optimization Techniques

A thesis submitted in partial satisfaction of the requirements for the degree of

Bachelor of Arts

in

Physics

by

Eric M. Fraser

Advised by:

Richard Mawhorter, Physics, Pomona College

David Tanenbaum, Physics, Pomona College

Charles Taylor, Chemistry, Pomona College

John Kaeding, Materials, University of California at Santa Barbara

Shuji Nakamura, Materials, University of California at Santa Barbara

May 2005

Table of Contents

List of Figures and Tables 3
1 Abstract 4
2 Introduction 6
2.1 Background 6
2.2 Motivation: ultraviolet applications 6
2.2.1 Biological agent detection 8
2.2.2 Communication 8
2.2.3 Lighting 9
2.2.4 Optical storage 13
2.3 Project overview 15
2.3.1 Material choices 15
2.3.2 Fabrication method 18
2.3.3 Characterization techniques 18
2.3.4 Research goal 20
2.4 Document overview 20
3 Theory 21
3.1 Background theory 21
3.1.1 Light emitting diodes 21
3.1.2 Crystallography 23
3.2 Lattice mismatch 30
3.2.1 Mismatch problem 31
3.2.2 Buffer layer 33
3.3 Crystal defects and dislocations 35
3.3.1 Threading dislocations (edge, screw) 36
3.3.2 Point defects (vacancy, interstitial, substitution) 41
3.3.3 Other types of defects 41
3.3.4 Sources of defects 42
3.3.5 Effects of defects 43
3.4 X-ray methods 44
3.4.1 On-axis measurements 46
3.4.2 Off-axis measurements 47
3.4.3 Device layer characterization 47
4 Equipment 52
4.1 Deposition reactor 52
4.2 Characterization equipment 53
4.2.1 X-ray diffractometer 53
4.2.2 Optical microscope 55
4.2.3 Scanning electron microscope 55
4.2.4 Atomic force microscope 55
5 Procedure 57
5.1 Deposition 57
5.2 Characterization 58
5.2.1 X-ray diffraction 58
5.2.2 Scanning electron microscopy 62
6 Analysis 63
7 Conclusions 72
8 References 73
9 Acknowledgements 78

List of Figures and Tables

Figure 1: Solar irradiance below earth's surface 9
Figure 2: Chromaticity 10
Figure 3: Spectra of white lights 12
Figure 4: SEM image of CD surface 14
Figure 5: Periodic table with relevant elements highlighted 15
Figure 6: Sapphire substrate (a) diagram, (b) photo 18
Figure 7: A *p-n* junction with (*a*) no potential, (*b*) forward bias 22
Figure 8: Transitions, (a) radiative, (b) non-radiative 23
Figure 9: Hexagonal crystal structure 24
Figure 10: Arbitrary unit cell 25
Figure 11: Hexagonal unit cell 25
Figure 12: Würtzite GaN structure 26
Figure 13: Sapphire unit cell 27
Figure 14: Hexagonal coordinate system 28
Figure 15: Common hexagonal (*a*) directions and (*b*) planes 30
Figure 16: Schematic of AlGaN on sapphire 33
Figure 17: Growth process of AlGaN on AlN template 35
Figure 18: Simple cubic lattice 36
Figure 19: Edge dislocation 37
Figure 20: Screw dislocation 37
Figure 21: Three dislocations form a loop 38
Figure 22: Three dislocations form a node 39
Figure 23: Typical sample for experiments 40
Figure 24: Vacancy and interstitial defects 41
Figure 25: Grain boundaries 42
Figure 26: X-ray diffraction axes and angles 46
Figure 27: Diffraction of x-rays by a crystal 49
Figure 28: Two-flow MOCVD process 53
Figure 29: Outside of x-ray diffractometer 54
Figure 30: Inside of x-ray diffractometer 54
Figure 31: Optical Microscope 55
Figure 32: Atomic force microscope 56
Figure 33: Radial dependence of XRD peaks 59
Figure 34: Cracking 63
Figure 35: Deposits 63
Figure 36: Cross-sectional SEM image of sample 64
Figure 37: AlN (002) XRD scan 65
Figure 38: AlN/AlGaN (102) XRD scan, $x_{Al} \approx 0.35$ 66
Figure 39: AlN/AlGaN (102) XRD scan, $x_{Al} \approx 0.10$ 67
Figure 40: AlN/AlGaN (102) XRD scan, $x_{Al} \approx 0.22$ 68
Figure 41: On-axis XRD comparison 70

Table 1: Ultraviolet light 7
Table 2: Energy and wavelength parameters for AlGaN materials 16
Table 3: Lattice and thermal expansion parameters for AlGaN materials 32
Table 4: On-axis AlN/AlGaN comparison 70

1 Abstract

Light emitting diodes (LEDs) and laser diodes (LDs) have many advantages over conventional light sources. Current commercial LEDs span the spectrum from IR to near-UV. There are a variety of applications for devices that extend into the deep-UV, including biological agent detection and optical storage. The nitride material system is a set of semiconducting compounds that have wavelengths that span a broad range, from yellow to deep-UV. AlGaN has a direct bandgap that extends into the deep-UV range; we will try to grow device-quality material, deposited epitaxially using metalorganic chemical vapor deposition on sapphire substrates.

AlGaN as a semiconducting material is relatively immature; the AlGaN MOCVD fabrication process is not yet optimized to produce high-quality material. As a result, current AlGaN optoelectronic devices suffer from low efficiency and short lifetimes due primarily to threading dislocations. Previously, there was no well-known method for quickly determining the dislocation density in AlGaN. Two techniques are conventionally used to characterize AlGaN: transmission electron microscopy (TEM) and X-ray diffraction (XRD). TEM is very time- and labor-intensive, however, and conventional XRD techniques did not work for AlGaN — the peaks were too broad relative to the peak separation to obtain quantitative data. Additionally, current AlGaN test devices use an AlN buffer layer between the substrate and AlGaN layer. Since AlN is relatively easy to characterize, current characterization techniques focus on the AlN buffer layer. I was not convinced, however, that there is compelling evidence to suggest that the AlGaN material quality is strongly linked to the AlN layer quality.

This project addressed both issues. That is, I created a new method to quickly characterize AlGaN material using XRD. The characterization method includes reducing the Al composition in the sample, taking an initial x-ray diffraction scan to determine this composition, then using that data to determine the expected diffraction angles. This method worked for roughly one third of the AlGaN samples. I used this technique to begin to establish a relationship between AlN quality and AlGaN quality. Reactor complications prevented a large data set for the AlN/AlGaN study, but initial data suggest that large changes in AlN quality (a 60% reduction in screw dislocations) correlate to significantly smaller changes in AlGaN material quality (a 20% reduction). This suggests that utilizing the novel characterization technique, resources should likely be used to optimize the AlGaN layer directly, since that is the active device region in LEDs.

2 Introduction

2.1 Background

A light-emitting diode (LED) is a semiconductor-based *p-n* junction. When a forward bias is applied, the diode emits light in a very narrow range of wavelengths. The first commercial LEDs were made from GaAsP in the 1960s and emitted red light at a wavelength of 655 nm (Marktech). In the decades that followed, the bulk of the visible spectrum could be covered by LEDs. Specifically, infrared LEDs through blue LEDs were commercially available by the mid-1990s, when Shuji Nakamura and his parent company, Nichia, released the first commercial GaN-based blue LED. Current technologies, based on GaN and InGaN, extend into near-UV, or the mid-300 nm range. This project is motivated by the push to make UV LEDs that extend deeper into the UV range.

2.2 Motivation: ultraviolet applications

Ultraviolet (UV) light spans a large portion of the spectrum, from roughly 10 nm to 380 nm. This range is typically broken up into smaller sections, as shown in Table 1. Contemporary LEDs span most of UVA; we hope to create LEDs that emit light in UVB and even UVC.

Table 1: Ultraviolet light

Range (nm)	Colloquial range	Type	Colloquial name
380-315	near UV	UVA	long wave (blacklight)
315-280	deep UV	UVB	medium wave
280-10		UVC	short wave (germicidal)

(Wikipedia, UV)

Deep-UV light sources and lasers have a wide variety of applications, including anthrax agent detection, corrective eye surgery (known by the trade name Lasik), water purification, and semiconductor lithography. Many of these applications could benefit from the compact and flexible form factor, high efficiency, low heat output, and relative inexpensiveness of LEDs and laser diodes (LDs). The current state of the art deep-UV laser is an XeBr excimer laser. Excimer lasers are very large (all required systems push the total size to greater than 1 m^3) and expensive, produce significant amounts of heat, and require extensive power and cooling systems. LDs eliminate or significantly reduce all of these problems. Thus, there is a strong incentive to produce laser diodes for these applications.

There are also a wide variety of specialty uses that require the unique benefits of LEDs and LDs, from communication to high-density optical storage. It is important to recognize that once the growth conditions and processing steps to make high quality LEDs are known for a given wavelength, only a few more steps are needed to make a laser diode (LD) at that wavelength. Additionally, a reverse-biased LED functions as a

photodiode at the same wavelength. These factors open up the realm of possible devices, so devices based on LDs and photodiodes are included in the following applications.

2.2.1 Biological agent detection

One of the primary reasons behind the push deeper into the UV range is the detection of biological agents, including, but not limited to, anthrax. Anthrax contains the compound tryptophan, which has a peak absorbance of ~280 nm. If a laser tuned to this frequency is pulsed and aimed at a sample containing tryptophan, the tryptophan will fluoresce with emitted radiation at a longer wavelength, which can be easily monitored (Carrano). Current anthrax detection methods use excimer lasers, but the disadvantages listed above prohibit widespread adoption. The low cost and size of an LD system would enable immediate, on-site detection in a variety of locations. Additionally, the size and power requirements would reduce the burden on the military to transport an excimer laser and the required power source.

2.2.2 Communication

Second in the list of possible applications is portable non-line-of-sight (NLOS) communication. 282 nm is in the solar-blind region of the spectrum, meaning that light at this wavelength (and at all wavelengths less than ~300 nm) is absorbed by the ozone in the earth's atmosphere (see Figure 1) (Parish 2001, 15). This provides two crucial benefits: 1) virtually no radiation originating outside the earth's atmosphere reaches the surface, and 2) virtually all radiation originating from the earth's surface is scattered and reflected back down to the surface. NLOS communication capitalizes on both of these features. Because the sun's radiation is blocked at this wavelength, there is extremely little background radiation, which enables a high signal-to-noise ratio, with transmitters

and receivers operating at relatively low power. The second benefit means that, simplifying things a great deal, a UV LD can be aimed in the general direction of a point in the sky between the source and the detector and its signal picked up by a reverse-biased LED (photodiode) some distance away. Due to the short range of UV light in the atmosphere (and unlike traditional RF communication devices), the range is limited to ~10 m – 250 m, which limits the possibility of long-range interception (SUVOS). This communication technique is not currently used, since the size of an excimer laser prohibits portable transmitters.

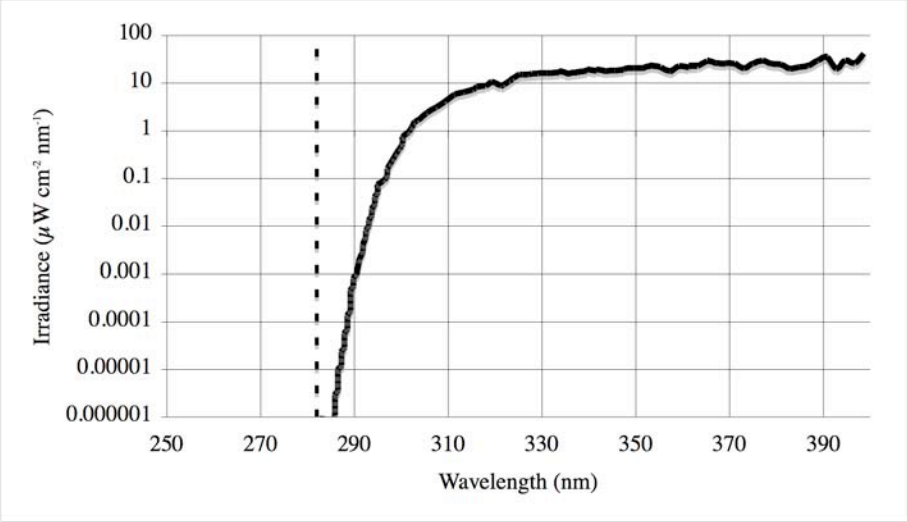

Figure 1: Solar irradiance below earth's surface

(dotted line at 282 nm)
(data from Parish 2001, 15)

2.2.3 Lighting

Perhaps the most widespread application for UV LEDs is general lighting. LEDs have demonstrated significant advantages over traditional lighting techniques, including incandescent, halogen, and fluorescent. Since white light is not a single wavelength, LEDs would seem to be ill suited for white light applications, since they have extremely narrow emission peaks. UV LEDs would seem to be even more ill-suited for these

applications, since the light output is not visible. Phosphors, however, can be used to absorb UV photons and emit photons in the visible range. Specifically, a mixture of europium and zinc sulfide doped with copper and aluminum gives off white light (Wikipedia, LED). This technique relies on the mixing of colors, as illustrated in the chromaticity diagram in Figure 2. The chromaticity diagram shown is the standard International Commission on Illumination (CIE, from its French name) figure. It represents a plot of visible colors of constant intensity. It is based on the additive principle, meaning that adding light on different axes gives the color in between the wavelengths in 2D space. In other words, one can see from the diagram that adding red, green, and blue light (from the three corners of the diagram) gives white light, as does adding yellow and blue (Fairchild 2005). This technique is analogous to the technique used in fluorescent sources. LEDs, however, can produce photons more efficiently than fluorescent bulbs.

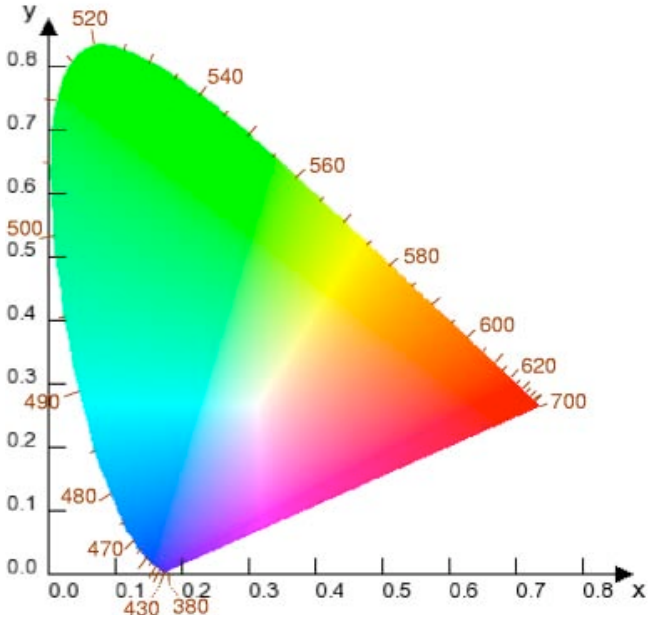

Figure 2: Chromaticity

(Elert)

First of all, LEDs convert a greater fraction of electrical energy to light and a correspondingly lower amount of heat. Figure 3 shows the spectrum of an incandescent bulb, with the visible range (400 nm – 700 nm) indicated by a box. The light at longer wavelengths is infrared and is wasted to heat. The gray line indicates the spectrum of a current white LED. Note that virtually no light is emitted outside the visible range. The heat reduction that LEDs make possible is significant for high-density applications, as well as general lighting — reducing heat output from general lighting can yield significant energy savings from cooling systems. LEDs are also extremely compact compared to traditional lighting techniques, which is a key concern in portable electronic devices. The expected lifetime of LEDs is $>10^6$ hours, orders of magnitude longer than that of conventional lighting, which is currently at $<10^3$ hours for incandescents and 10^4 hours for fluorescents (Nakamura 2000, VII). Additionally, LEDs typically do not suffer from instantaneous failure (burn-out), but rather the light output gradually declines, giving the user time to replace the bulb before it fails. LEDs can be dimmed easily, in contrast to fluorescent bulbs, and they can also be easily pulsed and turn on to full intensity virtually instantly. Finally, when mass-produced, LEDs have the potential to be cheaper than other light sources since there is no glass and relatively little mechanical assembly involved.

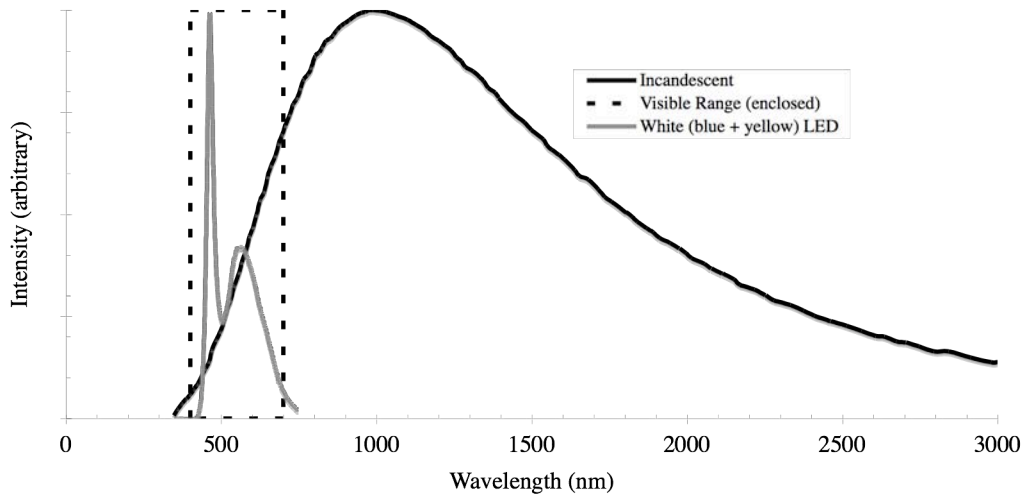

Figure 3: Spectra of white lights

(boxed region is visible range)
(data from Nichia)

The advantages listed above are models based on mature, colored LED technology. Achieving these gains awaits the maturation of the technology, specifically the material quality that this project is focused on. If the UV LED technology improves like colored LED technology has, white LEDs will exhibit similar advantages to the more established colored LEDs and will enable the realization of the advantages mentioned above.

White LEDs are currently commercially available but suffer from a significant problem. Most contemporary white LEDs use a blue emitter and a yellow phosphor. This causes the emission to have a very narrow blue peak and a somewhat broader yellow peak (see Figure 3). These peaks cause the color temperature of the light to be somewhat cooler than traditional lighting sources and also significantly limit the color rendering of the bulb. Color rendering is a measure of what colors look like when illuminated with a given

light source compared to a standard blackbody source. Lighting sources with poor color indices will not illuminate some colors well. For instance, green objects illuminated by a white LED bulb made with yellow and blue light will not appear as bright as when viewed under conventional lights. Using UV emitters with phosphors will improve both the effective color temperature and rendering of white LEDs.

2.2.4 Optical storage

Another application that has the potential for widespread consumer use is high-density optical storage. Optical storage is currently widely used in the form of CDs and DVDs, among other formats. The leap in storage capacity from the CD to the DVD was made possible by the use of a shorter wavelength laser source. CDs use 780 nm IR laser diodes; DVDs use 650 nm red LDs (combination CD/DVD players use dual LDs). Next-generation DVDs (based on both of the competing standards, HD-DVD and Blu-Ray) will use 405 nm blue lasers (Wikipedia, Blu-Ray Disc). Shorter wavelengths have a lower optical diffraction limit. Optical media is based on the recognition of very small features by a focused laser source. The storage capacity is based on the density of these features (commonly referred to as pits and bumps; see Figure 4). The diffraction limit determines how close the features can be from one another. Thus, since DVDs use a shorter wavelength laser source compared to CDs, DVDs have a higher density of pits and bumps, which means they can have greater capacities. Moreover, since the pits and bumps can be closer together in two directions, the storage gain is proportional to the square of the linear improvement:

$$\text{Capacity} \propto (\text{distance between features})^2 \qquad (1)$$

An additional jump in storage capacity, therefore, can be made with an even shorter wavelength laser source. A deep-UV LD would be perfectly suited for such a task.

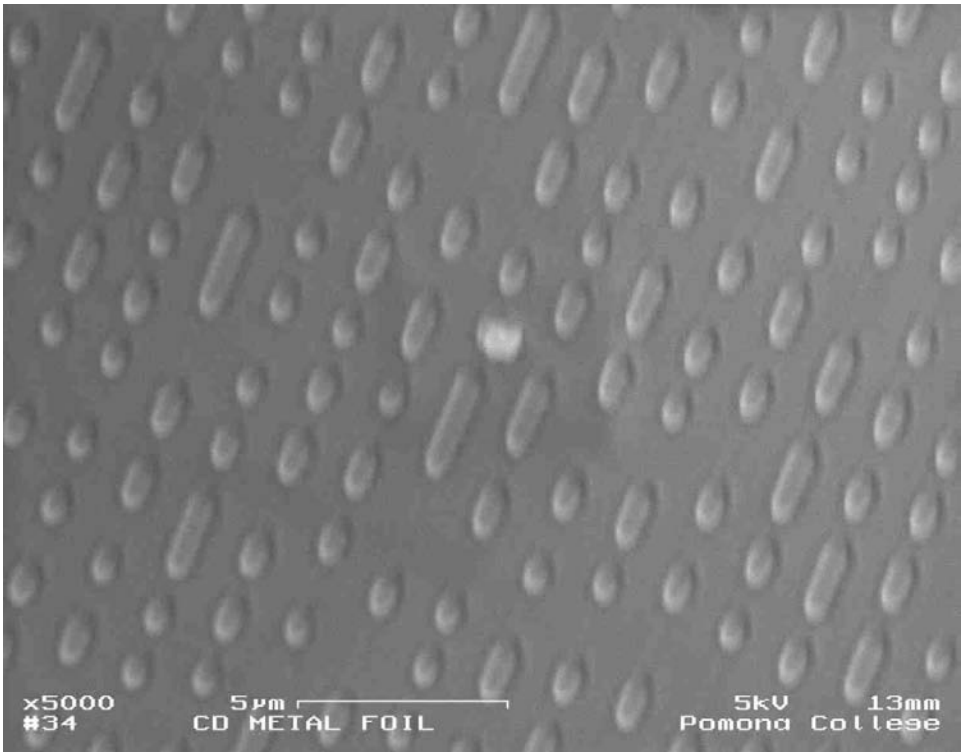

Figure 4: SEM image of CD surface
(Image courtesy of David Haley, Pomona College)

2.3 Project overview

2.3.1 Material choices

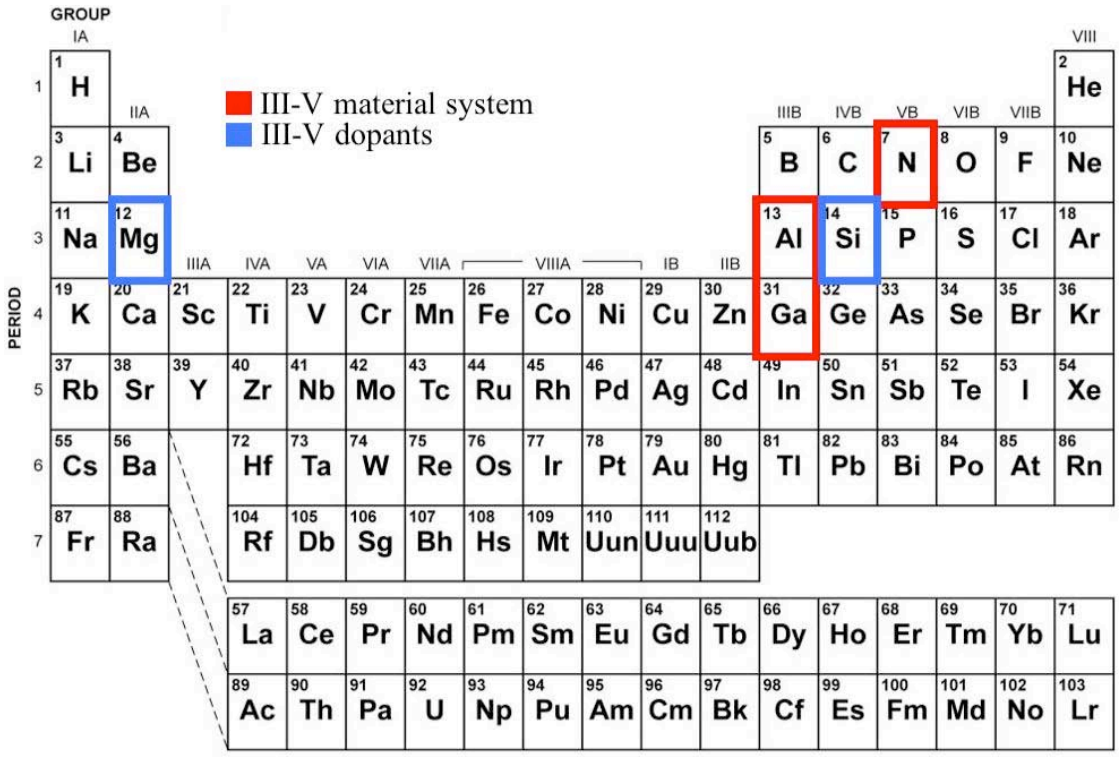

Figure 5: Periodic table with relevant elements highlighted
(Luidiauk)

Elemental semiconductors (*e.g.* Si, Ge) are not particularly useful in optoelectronic devices. They have a limited bandgap range and have indirect bandgaps. In the past decade, compound semiconductors, and specifically the III-V semiconductors — so named because of their positions in the periodic table — have gained increased importance in the semiconductor world. Three Group III Nitrides (III-Ns), (Al, Ga, In)N, are useful, and we will consider two of them, AlN and GaN, which are highlighted in Figure 5 above. For optoelectronic devices, the III-Ns have a direct bandgap, as well as a wide bandgap range with a corresponding wavelength range that spans from yellow to deep-UV. The III-Ns form continuous solid solutions, which enables the use of the full

bandgap range (Berger 1997, 123-34). Modern fabrication techniques such as metalorganic chemical vapor deposition (MOCVD), molecular beam epitaxy (MBE), and hydride vapor-phase epitaxy (HVPE) have enabled both research into and commercial devices from this family of materials.

This project focuses on AlN templates and AlGaN device layers grown on sapphire using Mg as a *p*-type dopant and Si as an *n*-type dopant (also highlighted in Figure 5 above). $Al_XGa_{1-X}N$ has a direct bandgap that ranges from 4.3 eV ($x = 0$) to 6.2 eV ($x = 1$), which corresponds to the wavelength range from 365 nm to 200 nm. This range contains 282 nm, the desired deep-UV wavelength. For the desired wavelength of 282 nm, $x = 0.35$ (see Table 2).

Table 2: Energy and wavelength parameters for AlGaN materials

	AlN	**GaN**	**$Al_xGa_{1-x}N$ $x = 0.35$**
E_g (eV)	6.2 eV	3.44 eV	4.4 eV
λ (nm)	200 nm	365 nm	282 nm

(Nakamura 2000)

The direct bandgap provides an advantage over semiconductors with indirect bandgaps because direct bandgap materials make significantly more efficient optoelectronic devices. In direct bandgap material, a photon is created by the transition of an electron between the valence and conduction bands (this process is discussed in more detail in section 3.1.1 below). In indirect bandgap material, a phonon must change the electron's momentum as it changes its energy level. The added requirement of the phonon reduces the efficiency since the probability of the interaction drops.

Since AlGaN has a hexagonal crystal structure, the substrate should ideally have a similar structure. AlN or GaN substrates would be ideal substrates since the lattices would match very closely, but to date no process has created bulk single-crystal AlN or GaN of sufficient size for use as substrates. Sapphire (Al_2O_3) and silicon carbide (SiC) are both hexagonal; both are currently being used as substrates in deep-UV LED research.

This project uses sapphire since it has several advantageous properties. First, sapphire is optically transparent in the UV range; this transparency allows light to be extracted through the substrate. For packaging concerns, this means either that mirrors can be placed behind the sapphire to reflect light back through the front of the LED or that it can be mounted upside-down (known as flip-chip mounting) so the sapphire surface becomes the front of the diode and the primary light source. Additionally, sapphire is less brittle than SiC, which allows for easier growth and processing steps. Finally, sapphire substrates are significantly less expensive than SiC substrates and cost is a key concern for consumer applications. We use 430 μm thick sapphire wafers 2 inches in diameter, as shown below. They are *c*-plane sapphire with a miscut of 0.15° toward the *m*-plane, supplied by Namiki Precision Jewel Co. The miscut improves the stepflow growth of the deposited layers (Hanlon 2003). One edge of each wafer is flat; this edge corresponds to an *a*-plane in the lattice.

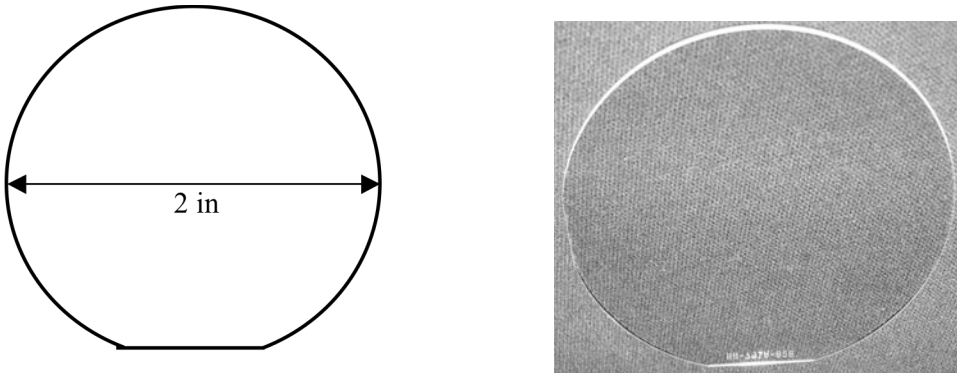

(a) (b)

Figure 6: Sapphire substrate (a) diagram, (b) photo

2.3.2 Fabrication method

The thin films for the LEDs are grown epitaxially (growth along the same crystal orientation) using metalorganic chemical vapor deposition (MOCVD). The primary alternative method to MOCVD growth is molecular beam epitaxy (MBE). MOCVD is a desirable method since it does not need to operate under a very high vacuum, while MBE growth requires such a vacuum. Hydride vapor-phase epitaxy (HVPE) is another fabrication method, but the high growth rates make it a non-ideal method for fabricating optoelectronic devices. Rather, HVPE is currently being used to investigate techniques to grow bulk GaN for substrates (Haskell 2005).

2.3.3 Characterization techniques

Several characterization techniques are used, with the two techniques discussed here being the most common. First among these is optical microscopy (see section 4.2.2). This technique gives rough estimates of surface quality and layer thickness, as well as a qualitative look at the surface. The second technique is single-crystal x-ray diffraction (XRD) (section 4.2.1). XRD allows us to determine the crystal structure quality. We can

also extrapolate XRD data to get relative measurements of dislocation densities. It is also possible to determine the relative compositions of aluminum and gallium in AlGaN layers using XRD.

Different techniques are also occasionally used. These include transmission electron microscopy (TEM), atomic force microscopy (AFM), and scanning electron microscopy (SEM). TEM, typically performed for us by other groups, is used to obtain quantitative dislocation density data, which is used to correlate to XRD data. SEM images are used to observe the layer structure. AFM gives quantitative data of surface morphology.

Each technique has advantages and disadvantages. SEM and optical microscopy do not give meaningful quantitative data about the material structure. AFM is useful only for the surface, which is not necessarily representative of deeper layers. TEM is a slow process that requires significant sample preparation and training. XRD is the most common characterization process to determine III-N material quality, since it provides quantitative data about the material, but it is less intuitive than optical, SEM, and AFM. It is more difficult to interpret the XRD data, and each new material system requires new derivations to determine appropriate diffraction angles.

Since we are interested in material quality, we will use XRD to characterize the samples because it is quicker. The gain from the initial investment of time to create new characterization techniques will be realized by the ability to characterize several samples in one day.

2.3.4 Research goal

The long-term goal is to make high-quality deep-UV LED devices. Since a number of years of research by many labs around the world have not yet yielded such devices, the goal for this particular project is less ambitious. Decades of experience indicate that semiconductor devices need high-quality material to be efficient and reliable. A key step in the process, therefore, is to determine what growth conditions yield the best material. This, in turn, brings the challenge of determining just how good the material really is. This project focuses on those issues— how to effectively characterize the material quality, and what the most efficient method is to optimize the material.

2.4 Document overview

This document serves two audiences. The first group is future students at Pomona and Santa Barbara. There is a long tradition of Pomona students continuing research that was started as a senior thesis project. Additionally, the Nakamura lab will likely take on future undergraduates in a role similar to mine. I hope that a student in either group would find this document helpful as both an introduction to the subject area and equipment, as well as serving as a place to pick up the research. I have structured the document to include an overview of the applications, theory, equipment, and problems encountered in my research.

Next, this is a scientific paper serving as my senior thesis — I will present this to the faculty at Pomona College. The dual nature of this paper, however, means that the latter group may choose to skip several sections, including 3.1, 3.2, 3.3, and 4.2 (background material science theory and standard characterization equipment). This group should,

however, pay particular attention to sections 3.4, 5.2.1, and 6 (my contributions to the theory and procedure, as well as my analysis).

3 Theory

3.1 Background theory

3.1.1 Light emitting diodes

LEDs are *p*-*n* junctions, as illustrated in Figure 7. They emit light through electronic excitation, or electroluminescence. In the operation of the LED, a forward bias is applied, which excites electrons from the *n*-side of the diode and holes from the *p*-side to move to the junction, where they recombine. Two types of recombination are possible: radiative recombination, when photons are produced, and non-radiative recombination, when phonons are produced. Figure 8 shows both forms of transitions. In radiative recombination, an electron in the conduction band drops in energy to the valence band, releasing this change in energy (equal to the bandgap E_g) as a photon, whose wavelength is given by Planck's formula,

$$\lambda = hc / E_g, \tag{2}$$

where h is Planck's constant and c is the speed of light. In non-radiative recombination, an electron falls into a trap in the bandgap and then falls again to recombine with a hole. In this case, the energy is released in the form of a phonon, not a photon. A phonon is a quantized vibration in the crystal lattice. It is the principal mode of thermal energy transport in solids and can be thought of as a short wavelength wave that propagates through the crystal at the speed of sound (Callister 2003, 657-59). Instead of producing

light, as in the case of a photon, a phonon produces heat, thereby reducing the efficiency of the device. The traps in this case are formed from impurities in the crystal lattice, which is why high-quality material leads to more radiative recombination, and thus greater efficiency (Nakamura 2000, 2.8.1). A more detailed description of the processes that cause non-radiative recombination is given in section 3.3.5 below.

Laser diodes function in a similar way, but require amplification and a resonant cavity. A more thorough discussion of the laser diode is available in a number of sources (e.g. Nakamura 2000, 2.8.2). For our purposes, the similarities between LEDs and LDs are more important than the differences — in both devices, non-radiative combination is the result of lattice imperfections and occurs at the expense of radiative combination (Fraser 1977, 92-93).

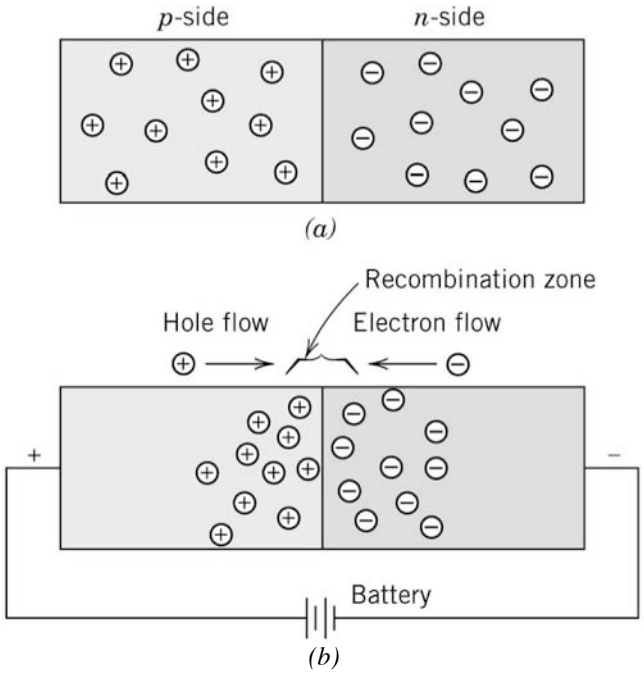

Figure 7: A *p-n* junction with (*a*) no potential, (*b*) forward bias
(Callister 2003, 636)

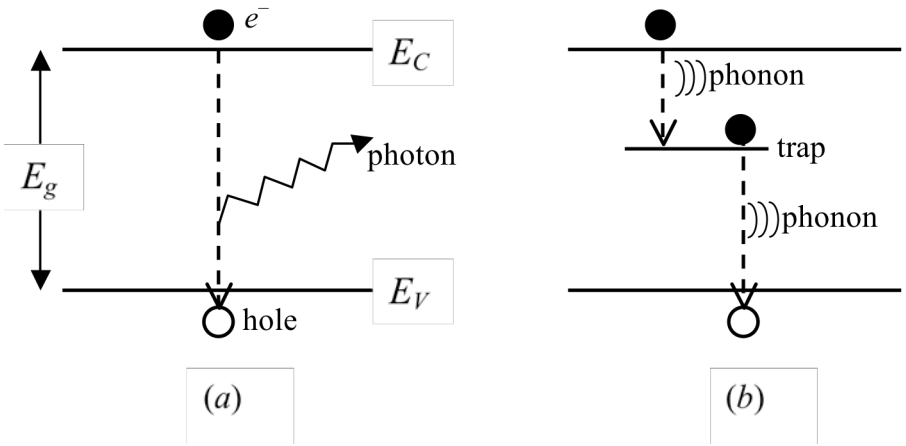

Figure 8: Transitions, (a) radiative, (b) non-radiative

3.1.2 Crystallography

A material is crystalline if its atoms are arranged in a regular, repeating pattern. A single crystal is one where there is an uninterrupted periodic pattern to the atomic arrangement. Each crystal has a specific crystal structure that describes the spatial arrangement of the atoms. The crystal lattice is the three-dimensional array that describes the structure. Not coincidentally, all of the materials used in our samples have the same basic crystal structure. GaN and AlGaN typically crystallize in the hexagonal würtzite structure, but can also crystallize in the cubic zinc-blende phase (Garni 1996). The GaN and AlGaN in this project will be exclusively würtzite. The hexagonal würtzite structure describes a lattice of atoms that are arranged in a regular hexagonal pattern in each plane (Figure 9).

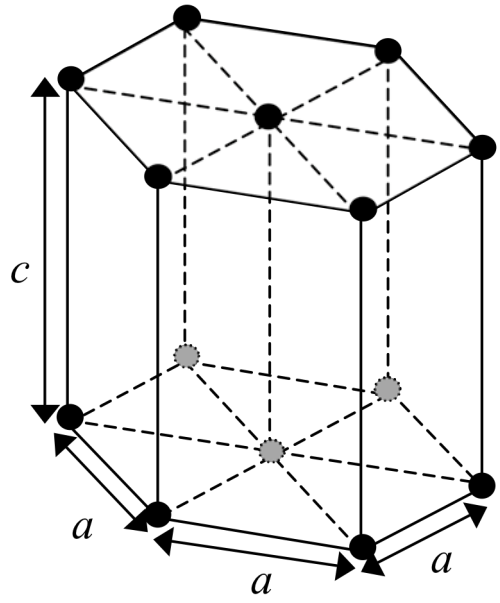

Figure 9: Hexagonal crystal structure

Since crystals are periodic, we can define one arrangement of atoms that, when regularly translated, can represent a crystal of arbitrary size. This arrangement is called the unit cell and is typically a parallelepiped whose corners coincide with the centers of atoms in the crystal. From this unit cell, we can define an x, y, z coordinate system along the edges of the unit cell. The sides of the unit cell are then defined to have lengths a, b, and c. It should be noted that the coordinate system defined by the parallelepiped is not necessarily, and often is not, orthogonal. The angles between the axes, then, are described by the angles α, β, and γ. Figure 10 shows these axes, lengths, and angles for an arbitrary unit cell. Figure 11 shows the unit cell for a hexagonal crystal system (note the shaded area in Figure 11, which is distinct from Figure 9). The hexagonal system is described by the following relationships:

$$a = b \neq c$$
$$\alpha = \beta = 90°,\ \gamma = 120°. \tag{3}$$

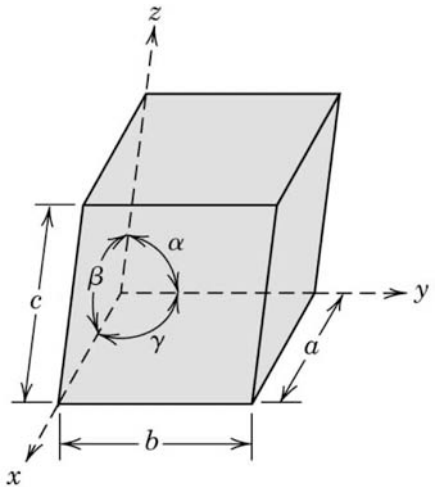

Figure 10: Arbitrary unit cell
(Callister 2003, 39)

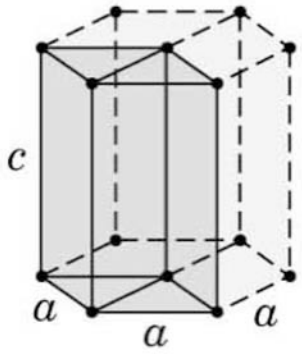

Figure 11: Hexagonal unit cell
(Callister 2003, 40)

The III-N material system and sapphire are not simple hexagonal structures, however. The complete lattice is described below. However, for the purposes of this project, the approximation of both types of materials to a simple hexagonal system as shown in Figure 9 and the corresponding unit cell shown Figure 11 is appropriate and will be used exclusively hereafter.

The würtzite structure (GaN, AlN, AlGaN) is composed of two interpenetrating hexagonal sub-lattices that are offset from one another by ~1/3*c* in the direction parallel to the *c*-axis. This structure is shown for GaN in Figure 12. For AlN, the Ga atoms are replaced by Al. The AlGaN structure follows the same form, but depends on the composition. The Al_2O_3 sapphire structure is more complicated (Haskell 2005 and Evans 1966, 166-75). As described by Haskell, “the structure can be thought of as a hexagonal

. . . oxygen lattice with two-thirds of the tetrahedral interstices occupied by aluminum atoms" (Haskell 2005). The unit cell of this structure is shown in Figure 12.

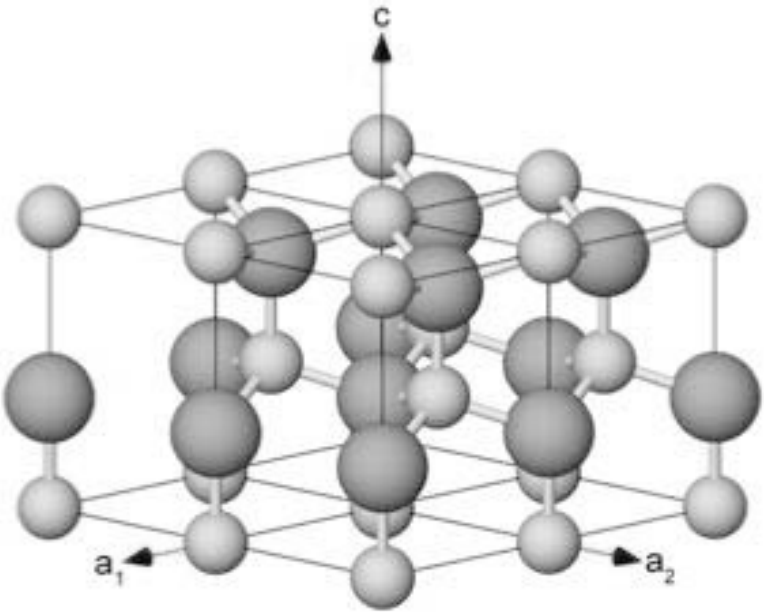

Figure 12: Würtzite GaN structure

(Lighter atoms are Ga; darker atoms are N)
(Haskell 2005)

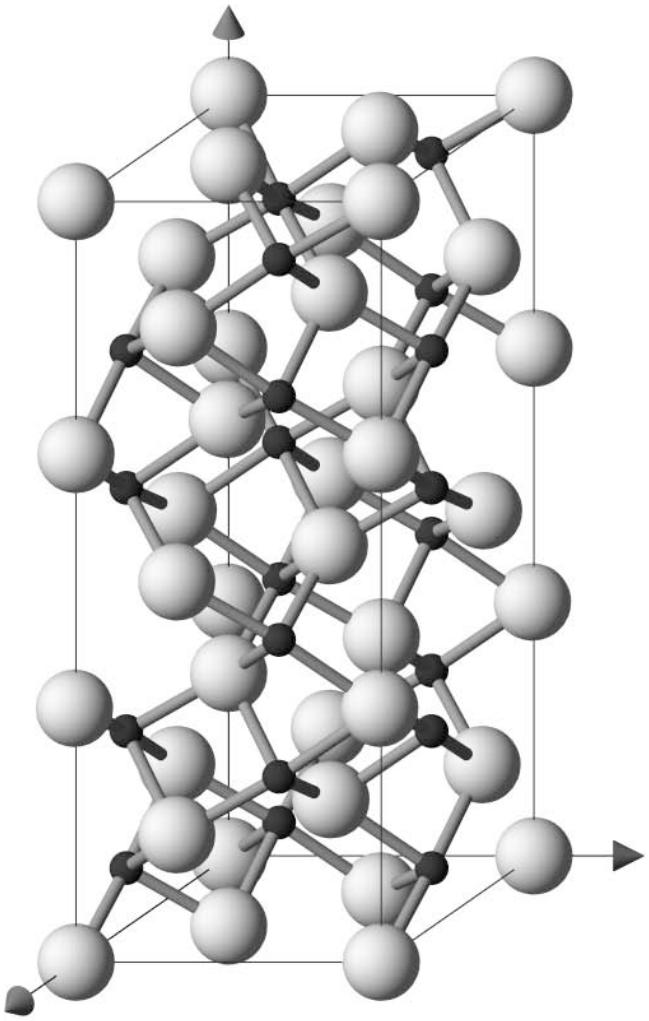

Figure 13: Sapphire unit cell

(Lighter atoms are O; darker atoms are Al)
(Haskell 2005)

Directions in a crystal are typically defined as vectors that pass through the origin of the unit cell. The length of the vector is given in terms of *a*, *b*, and *c*. The vector is conventionally expressed in terms of components in the *x*, *y*, *z* directions that are enclosed in square brackets without commas or any other punctuation: [*uvw*], where *u*, *v*, and *w* correspond to the projections along the *x*, *y*, and *z* axes, respectively. Negative coordinates are indicated by bars above the corresponding index, *e.g.* [1$\bar{1}$1]. The

components of the vector are always scaled by a common factor to be the smallest possible integer values.

Since hexagonal crystal systems have six-fold symmetry, there is a more intuitive vector system for these systems. The four-axis Miller-Bravais coordinate system describes three vectors (a_1, a_2, and a_3) in a single plane that form angles of 120° between each other. The z-axis is then perpendicular to this plane, as shown in Figure 14.

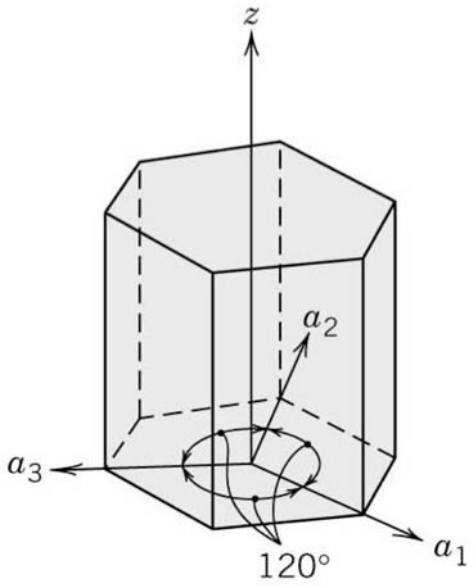

Figure 14: Hexagonal coordinate system

(Callister 2003, 45)

The transformation between three-axis notation and four-axis notation

$$[u'\ v'\ w'] \rightarrow [uvtw] \tag{4}$$

is given by the following relationships (where n is a factor that may be required to scale the resulting vector so its components are the smallest possible integers):

$$\left.\begin{aligned} u &= \frac{n}{3}\left(2u' - v'\right) \\ v &= \frac{n}{3}\left(2v' - u'\right) \\ t &= -\left(u + v\right) \\ w &= nw' \end{aligned}\right\} \tag{5}$$

(Callister 2003, ch. 3; Cullity 2001 ch. 2).

The representation of crystallographic planes follows a similar pattern and is of particular interest to this project, since understanding x-ray diffraction relies on crystallographic planes. Planes are described by Miller indices *h*, *k*, and *l*, and notated inside closed parentheses with no other punctuation: (*hkl*). Each plane in a crystal intersects all three axes (unless it passes through the origin, in which case a parallel plane or a different unit cell should be chosen for the calculations). Each Miller index is defined to be the reciprocal of the distance between the origin and the intersection of the plane along the corresponding axis, given in terms of the appropriate lattice parameter *a*, *b*, or *c*. The indices are always scaled to integers, but, unlike the notation for vectors, the indices for planes are not always scaled to be the *smallest* possible set of integers. For x-ray diffraction, the particular plane is important — (001) is not the same as (002). As in vector notation, a bar over an index indicates an intercept on the negative side of the corresponding unit cell.

Once again, hexagonal planes can be described in terms of the alternate Miller-Bravais four-axis coordinate system, in the form (*hkil*). The transformation between three-index and four-index planes is simpler than the transformation for vectors. The *h*, *k*, and *l* indices are the same in both three- and four-index systems; *i* is given by

$$i = -(h + k). \quad (6)$$

We will adopt the more familiar three-index Miller system. Common hexagonal crystal directions and planes are shown (using four-index notation for reference) in Figure 15 (Callister 2003, ch. 3; Cullity 2001 ch. 2).

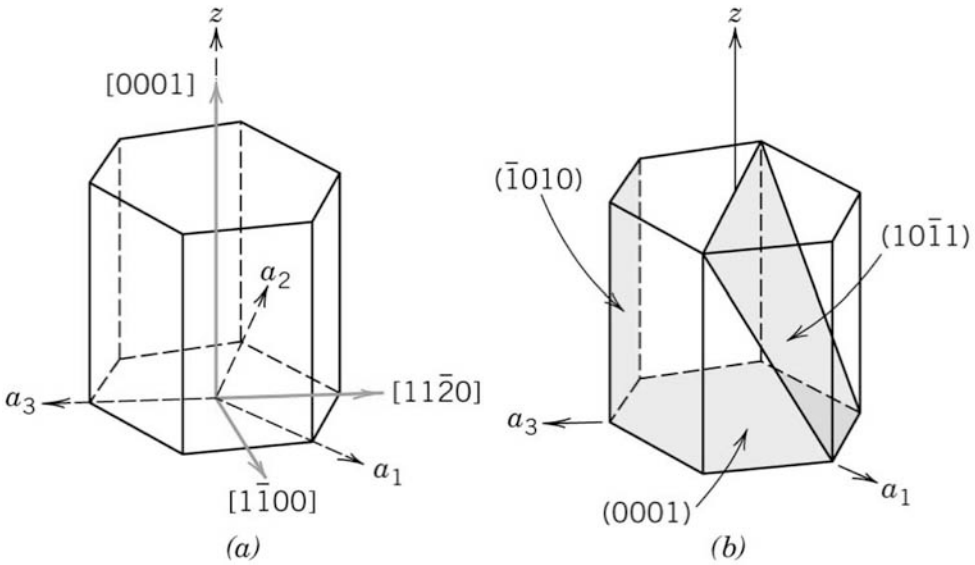

Figure 15: Common hexagonal (*a*) directions and (*b*) planes
(Callister 2003, 46)

3.2 Lattice mismatch

Epitaxial growth of one material on a dissimilar substrate presents many challenges. These problems are the result of differences in the lattice parameters and the coefficients of thermal expansion (CTE) for each layer. The lattice mismatch will stress the deposited layers; the CTE mismatch will cause additional strain when the sample temperature changes (as is always the case during CVD film growth).

The lattice mismatch problem is analogous to the following situation. The common children's building block toy Lego has several competitors, Tyco among them. If a child

were to try to build a structure using layers of building blocks, he would run into difficulty if he tried to stack Tyco blocks on top of a Lego base layer. By pressing hard, he may be able to force the two layers together. One of the layers will be under tension and the other will be under compression. While the Lego structure may be able to withstand these forces for a small number of foreign Tyco blocks, adding a significant number of Tyco blocks (multiple layers) will amplify the forces on the structure. After adding a few additional blocks, the structure will likely bow and possibly crack.

3.2.1 Mismatch problem

At the atomic level, the mismatches in the lattices and CTE parameters can have disastrous effects on devices. As is the case with the building block example, the samples can develop curvature and can crack. Less critical failure is also possible. Non-relaxed crystal mosaics adversely affect the optical and electrical properties of a sample relative to relaxed samples, as will be discussed in section 3.3.5 below.

Table 3 shows the lattice and thermal expansion parameters for the materials that make up the layers in our samples. Our samples use *c*-plane sapphire — that is, the *c*-plane is the plane on which the layers are deposited. This means that the atomic spacing on this layer is actually given by the *a* lattice parameter.

Table 3: Lattice and thermal expansion parameters for AlGaN materials

	Sapphire	**AlN**	**GaN**	**$Al_xGa_{1-x}N$ $x = 0.35$**
***a* (at 300 K) (Å)**	4.76	3.112	3.189	3.16
***c* (at 300 K) (Å)**	12.99	4.982	5.185	5.11
***a*–CTE ($x10^{-6}$/K)**	7.5	5.3	5.59	
***c*–CTE ($x10^{-6}$/K)**	8.5	4.2	7.75	

(Nakamura 2000)

Simply examining the parameters in this table would lead to the conclusion that the lattice mismatch between sapphire and AlGaN is about 33%. If we superimpose the AlGaN lattice and rotate it by 30° relative to the sapphire lattice, the atoms line up much better. Figure 16 shows this arrangement. To calculate the lattice mismatch in this configuration, we use a geometrical argument. We will focus our attention on the four bottommost AlGaN and sapphire atoms. In this configuration, the spacing between sapphire atoms is still given by a_{Sapphire}, but the spacing of the AlGaN atoms is not a_{AlGaN}, even though the nearest-neighbor atoms in the AlGaN lattice are spaced by a_{AlGaN}. If we form a triangle around these two bottommost atoms that has its third point on the atom directly above one of those two atoms, as shown in the figure, we notice that the length of the shortest side is given by a_{AlGaN} and the length of the hypotenuse is given by $2a_{\text{AlGaN}}$. Applying the Pythagorean theorem, we find the spacing d between the two AlGaN atoms:

$$d^2 = a_{\text{AlGaN}}{}^2 + 2a_{\text{AlGaN}}{}^2 \Rightarrow d = \sqrt{3}\ a_{\text{AlGaN}}. \tag{7}$$

Rotating the lattice and introducing the factor of $\sqrt{3}$ reduces the lattice mismatch to about 15%. This is the lattice mismatch typically reported in the literature.

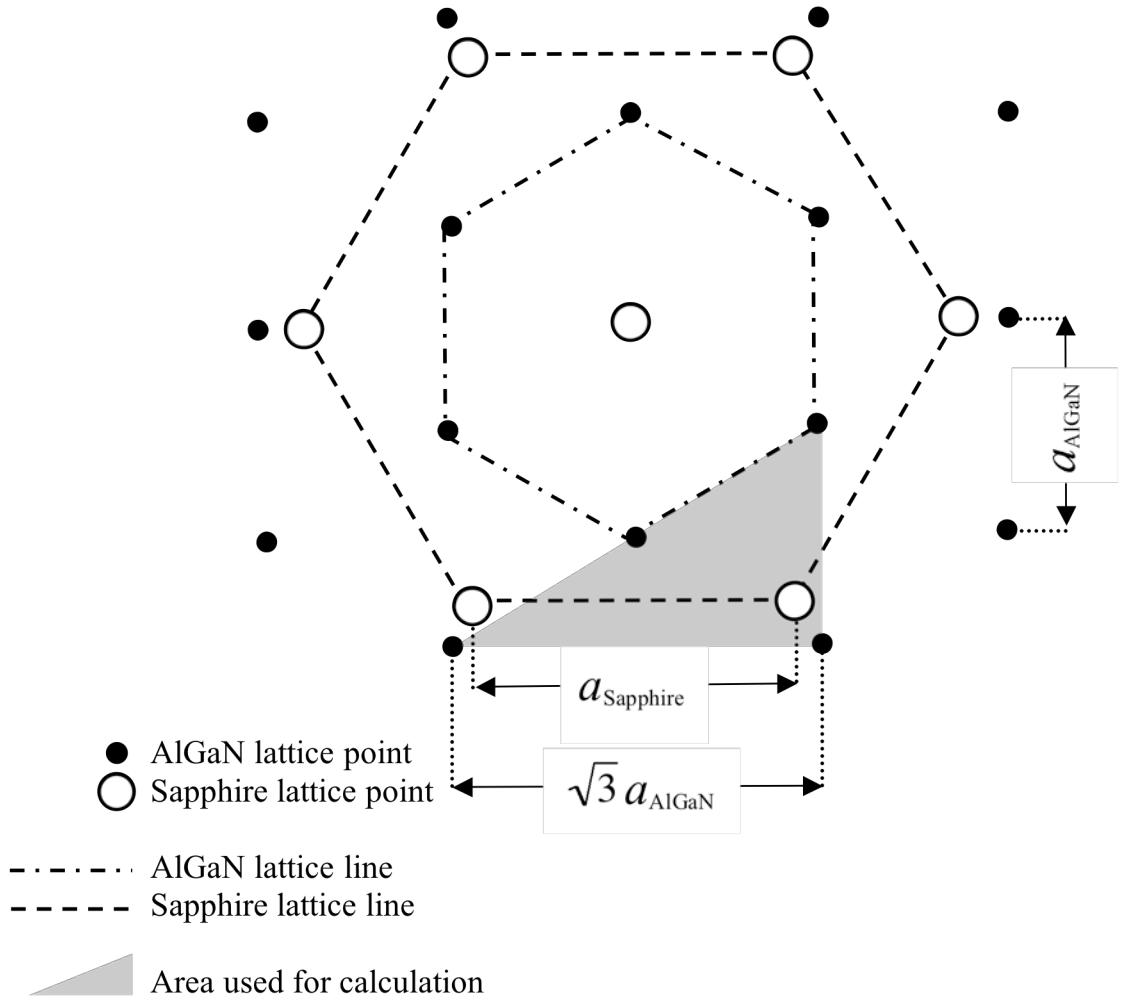

Figure 16: Schematic of AlGaN on sapphire

3.2.2 Buffer layer

As Table 3 shows, the lattices of sapphire and AlN are more closely matched than the lattices of sapphire and either GaN or AlGaN. This implies that AlN layers on sapphire will be under less stress than GaN (or AlGaN) layers on sapphire. The AlN lattice is closely matched to GaN, however, so growing AlGaN on an AlN layer presumably causes the resulting layer to be under less tension than if it were grown directly on sapphire.

We can therefore reduce the stress in the device layers by depositing a thin AlN template layer on the sapphire substrate to serve as a buffer between the sapphire and the AlGaN device layers (Akasaki 1989). A GaN template layer has many of the same beneficial properties as an AlN layer. GaN absorbs at 282 nm, however, which eliminates the possibility of extracting light out the back of the device (Kaeding 2004). Since using layers that absorb at 282 nm effectively halves the power output of the LED, we use AlN templates and sapphire substrates.

The growth on the AlN template described above involves four different processes. Nakamura describes these processes for GaN, which we can extend to AlGaN:

1. Island growth of GaN around nucleation sites of the AlN buffer layer
2. Lateral growth of GaN islands
3. Coalescence of lateral growth
4. Quasi-two-dimensional growth of GaN.

(Nakamura 2000, 61). These processes are shown in Figure 17.

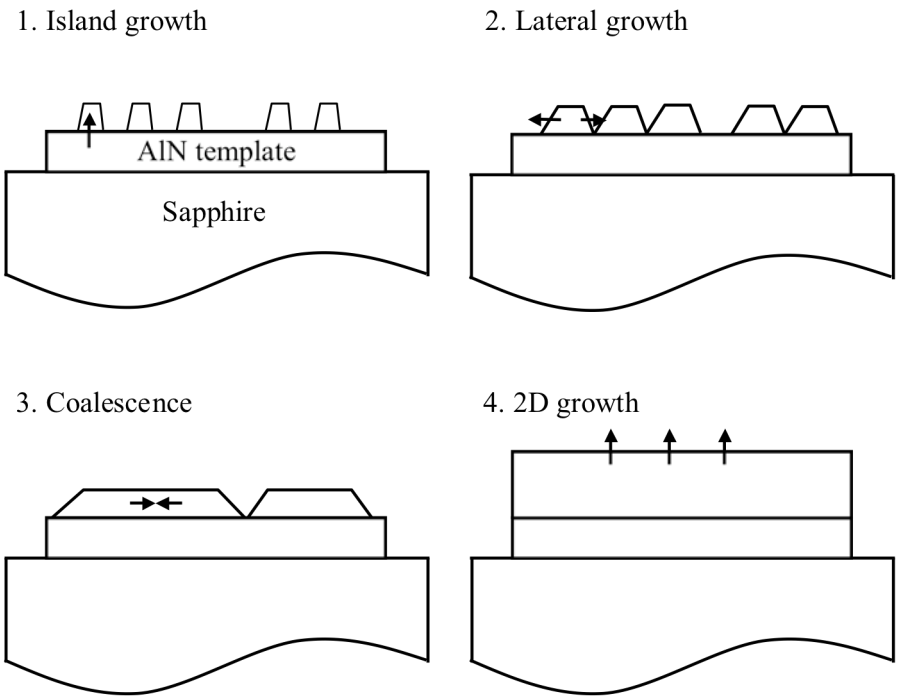

Figure 17: Growth process of AlGaN on AlN template
(Nakamura 2000, 62)

Fundamentally, the AlN layer supplies the AlGaN layer with nucleation centers with the same orientation. Recall from the previous section that the growth of AlGaN on sapphire requires a 30° misalignment between the layers. AlGaN, however, can grow directly on AlN of the same orientation. AlGaN deposits form crystals on these nucleation points, which then grow laterally, or parallel to the substrate, as shown in the first two steps of Figure 17. This lateral growth and resulting coalescence form AlGaN material that is one level removed from the large lattice mismatch between AlGaN and sapphire.

3.3 Crystal defects and dislocations

The overall goal of this project is to produce high-quality material — that is, free of defects in the crystal structure. To this end, we must know what defect-free structures

look like. For simplicity in this discussion, we will model atomic lattices as lattices formed by cubic structures. The discussions that will be presented extend to the hexagonal structure found in our materials.

Figure 18 below shows a perfect simple cubic lattice (with an arbitrary unit cell outlined). In this arrangement, the atomic spacing is uniform over the entire sample; the angles between atoms are also uniform.

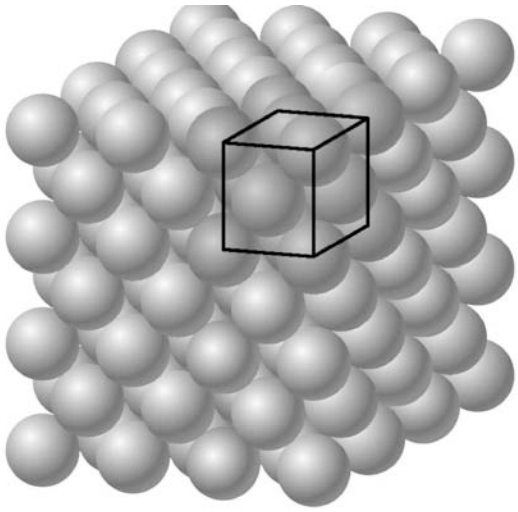

Figure 18: Simple cubic lattice
(Callister 2003, 70)

There are two primary types of crystal defects that plague our samples: threading dislocations and point defects. Threading dislocations include both edge and screw dislocations; point defects include vacancies, interstitial atoms, and substitutions (Hull 1965, 12-15).

3.3.1 Threading dislocations (edge, screw)

Both types of threading dislocations start from the presence of shear stress in the crystal lattice. A partial plane of atoms in between two planes of atoms in a lattice forms an edge

dislocation in the lattice (see Figure 19). The resulting distortion around the dislocation displaces the surrounding atomic planes and causes bending in the lattice. When atomic planes are shifted laterally with respect to other planes in the lattice, a screw dislocation occurs (see Figure 20).

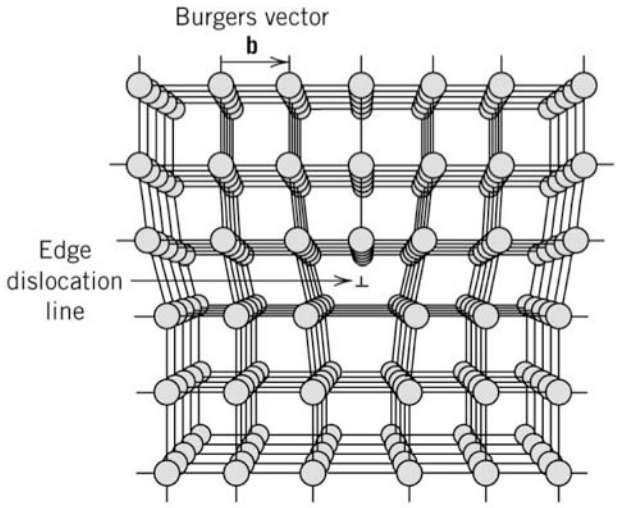

Figure 19: Edge dislocation
(Callister 2003, 74)

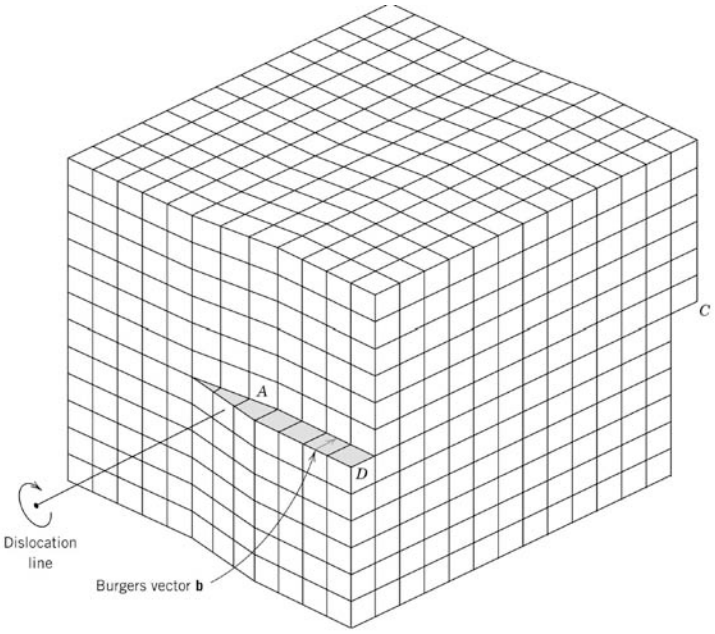

Figure 20: Screw dislocation
(Callister 2003, 75)

A Burgers vector **b** indicates the magnitude and direction of the lattice dislocation. For an edge dislocation, **b** is always normal to the dislocation line; for a screw dislocation, **b** is always parallel to the dislocation line (**b** is indicated in Figure 19 and Figure 20).

As a rule, dislocations do not terminate inside a single crystal lattice. They can terminate at the interface between two crystals, at the interface between a crystal and a non-crystal region (such as air), or at a grain boundary (where a domain of one orientation meets a domain of a different orientation). While they cannot terminate inside a single lattice, three or more connected dislocations can form a closed loop, as shown in Figure 21. Additionally, dislocations can branch out, represented by three Burgers vectors that meet at a point (a node) (see Figure 22). At each node, the sum of the Burgers vectors must be zero, analogous to conservation of momentum (Hull 1965, 16-20). In other words, if a dislocation represented by $\mathbf{b}_1$ branches into dislocations represented by $\mathbf{b}_2$ and $\mathbf{b}_3$, the following condition must be met:

$$\mathbf{b}_1 + \mathbf{b}_2 + \mathbf{b}_3 = 0 \Rightarrow \mathbf{b}_1 = \mathbf{b}_2 + \mathbf{b}_3. \quad (8)$$

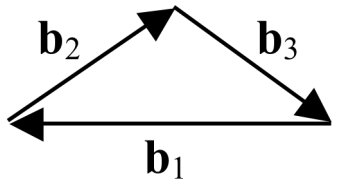

Figure 21: Three dislocations form a loop

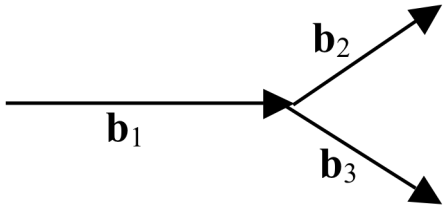

Figure 22: Three dislocations form a node

These conditions are critical to this project. While the loop and node concepts are not used directly, it is important to note that there is a fixed set of conditions that limits how dislocations can propagate and terminate. Specifically, we are interested in whether the dislocations terminate at material interfaces.

Our simplest sample for experimentation (Figure 23) contains three main crystals: the sapphire substrate, the AlN template, and the AlGaN device layer (a cross-sectional SEM image of this type of sample is in Figure 36 below). We know that both the AlN and AlGaN layers have a high density of dislocations. We want to reduce the dislocations, but each layer requires different optimization techniques. Since the optimization process can take significant resources (both time and money) for any material, we want to devote resources to optimizing the layer that will yield the best results.

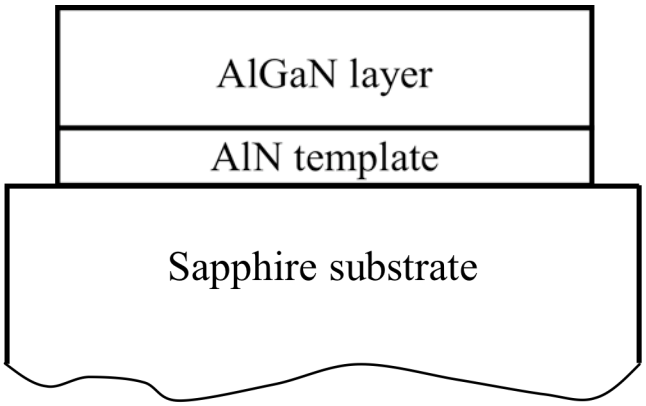

Figure 23: Typical sample for experiments

The dislocations' adverse effects on devices as discussed in section 3.3.5 are relevant primarily in the AlGaN device layers, but optimizing the AlN layers appears to be significantly easier than directly optimizing the AlGaN layers, for a variety of reasons. For example, as discussed in section 3.4 below, complete XRD scans are significantly easier on AlN layers than on AlGaN layers. Since XRD scans are our primary method for determining the dislocation content of our samples, this is an important consideration. The fact that the AlN template layer is highly dislocated may mean that any layer deposited on top of that layer would also be dislocated. If this is the case, optimizing the AlN layer should yield a more optimized AlGaN layer. On the other hand, the dislocations in the AlN layer may terminate at the AlN-AlGaN interface, which would indicate that resources should be diverted from AlN optimization to AlGaN optimization. This possibility stems from the rules describing dislocation propagation and termination above.

The quality of our samples, as partially characterized by dislocations, is an important part of the project. A compact, quantitative measurement of the dislocations would be ideal.

The most useful quantity is the dislocation density *N*. This density is defined as the total length of dislocations *l* per unit volume:

$$N = l/V, \tag{9}$$

Where *V* is the volume as measured in cm^3. Note that *N* refers to the dislocation *density*, not the number of dislocations. Additionally, the dislocation density is defined in terms of the total length of the dislocations, not the number of dislocations. *N* has units of cm^{-2}.

3.3.2 Point defects (vacancy, interstitial, substitution)

Point defects can take many forms. Vacancies occur when an atom is missing in the lattice. Interstitial atoms are atoms that occupy non-atomic sites in the lattice (both types of defects are illustrated in Figure 24). Substitutions occur when one kind of atom takes the place of another in the lattice. It is important to note that interstitial atoms and substitutions can be either impurity atoms or atoms usually present in the structure.

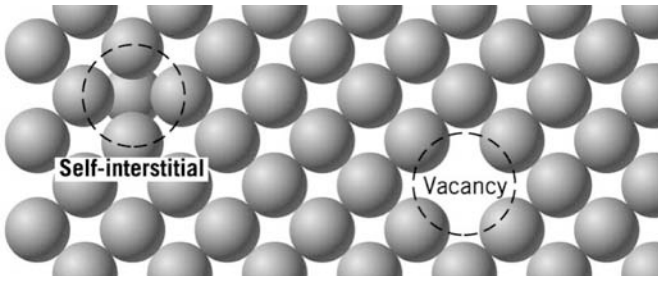

Figure 24: Vacancy and interstitial defects
(Callister 2003, 67)

3.3.3 Other types of defects

Many other types of defects can occur in crystals. These include, but are not limited to, the following: stacking faults, in which the regular pattern of atomic planes is interrupted,

and grain boundaries, when a lattice of one orientation meets a lattice of a different orientation (Figure 25).

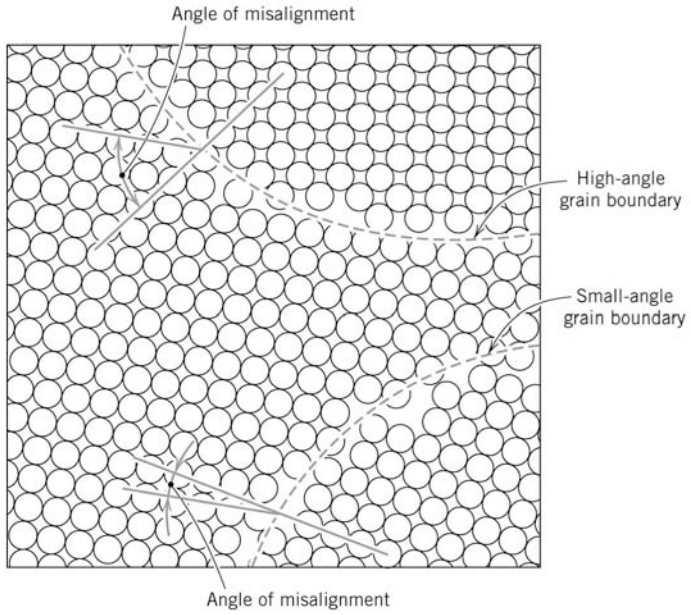

Figure 25: Grain boundaries
(Callister 2003, 78)

3.3.4 Sources of defects

As discussed above, the threading dislocations are the result of stress caused by the lattice mismatch between the substrate and device layers. There are several sources of impurity atoms. The primary impurities in the films are carbon and oxygen. Both elements can enter the system through the precursors and the carrier gases (Parish 2001). Additionally, oxygen is naturally in the trace water vapor left in the reactor even after bake-outs and pump-downs. Additionally, InGaN films are also grown in the same MOCVD reactor, so indium is a possible contaminant.

3.3.5 Effects of defects

Since GaN is a more mature optoelectronic material system than AlGaN, significantly more literature exists for studies of GaN than studies of AlGaN. Experiments have shown that defects affect AlGaN and GaN devices similarly. Since this analogy seems to hold, and due to the volume of knowledge of GaN-based devices, we will present some evidence focused on GaN devices and extend the discussion to include AlGaN devices.

Defects in GaN films on sapphire have been shown to have adverse effects on many properties of GaN-based devices. First, the defects affect the structural characteristics of the films, which, as described in section 3.4, will become our primary method for determining the defect density in our films (Heying 1996). Defects also affect the optical performance of GaN-based devices. Specifically, threading dislocation sites cause non-radiative recombination, which causes a deficiency of minority carriers, and, as a result, dark spots in the device (Rosner 1997). The dislocations create traps that cause this non-radiative recombination (Brazel 1999). Threading dislocations also form Coulomb scattering centers which form repulsive potential bands that bend around the dislocations, causing low transverse charge carrier mobility (Weimann 1998). In fact, there is evidence that there is a higher negative charge concentration near dislocations (Hansen 1998).

Dislocations decrease both the efficiency and the lifetime of a device. Extremely high dislocation densities can prevent the device from emitting light at all. Fortunately, since dislocations are fundamentally physical tiltings and twistings of the material, we can use

characterization techniques that reveal imperfections in the crystals to quantitatively determine the dislocation densities.

3.4 X-ray methods

Our focus here is primarily on threading dislocations. These dislocations are defects in the crystal structure and are thus detectable by x-ray diffraction. Specifically, as related to the quantitative TEM data on dislocations, the full width at half maximum (FWHM) of rocking curve peaks is roughly proportional to the dislocation density *N* (Heying 1996). Recall from (9) that the dislocation density depends on the total length of dislocations per unit volume. Since no TEM was conducted on the samples used in this project, we will not report quantitative values of *N*. Rather, it should be noted that a broader peak indicates a higher *N* and a narrower peak indicates a lower *N*.

As discussed in section 3.3.1, however, there are two different types of dislocations; each type deforms the lattice in a different direction. Specifically, edge dislocations tilt the lattice about the substrate normal; screw dislocations twist it about the normal. Hence, a single XRD measurement cannot distinguish between these two types of dislocations. Two XRD scans should reveal the dislocation density for both types of dislocations: one in the (001) direction (normal to the substrate), and one in the (100) direction (parallel to the substrate) (Heying 1996).

Of course, not all planes can be seen by the diffractometer. The visible planes are dependent on the reciprocal lattice and the Ewald sphere. A complete discussion of visible planes and a table of such planes is available from a variety of sources (*e.g.*

Cullity 2001 §3.4 – 3.6 and Cullity 2001 Appendix 9, respectively). In general, for a hexagonal structure, the following planes have detectable reflections:

$$h + 2k = 3N \text{ with } l \text{ even} \quad (10a)$$

$$h + 2k = 3N \pm 1 \text{ with } l \text{ even or odd.} \quad (10b)$$

The following planes have no detectable reflections:

$$2 + 2k = 3N \text{ with } l \text{ odd} \quad (11)$$

(Suryanarayana 1998, 59).

For our purposes, we will only discuss allowable diffraction planes. It is important to note that there are multiple diffraction planes that are parallel to each other and are allowed. For instance, (002) and (004) are parallel to each other and are both visible diffraction planes for AlN. In these cases, diffraction planes with lower Miller indices yield greater intensity. This means that a (002) scan can be taken faster (changing the angles more quickly) and can take less time to get the same signal-to-noise ratio and intensity compared to a (004) scan.

Figure 26 shows the axes and angles used by an x-ray diffractometer. The *x*, *y*, and *z* axes are standard Cartesian axes with the origin at the center of the stage in its home position. The *x*-axis is parallel to the door of the diffractometer. The stage can move in all three directions. The angle ϕ rotates the sample about the normal to the stage. ψ rotates the sample about a line parallel to *y*-axis. In practice, the diffractometer adjusts ψ by moving the stage in an arc in a plane normal to the *y*-axis. Changing ω rotates the sample about the *x*-axis. In practice, the diffractometer rocks the stage, which gives rise to the name

rocking curve for ω-scans. Finally, 2θ is the angle between the incident x-ray beam and the diffracted x-ray beam.

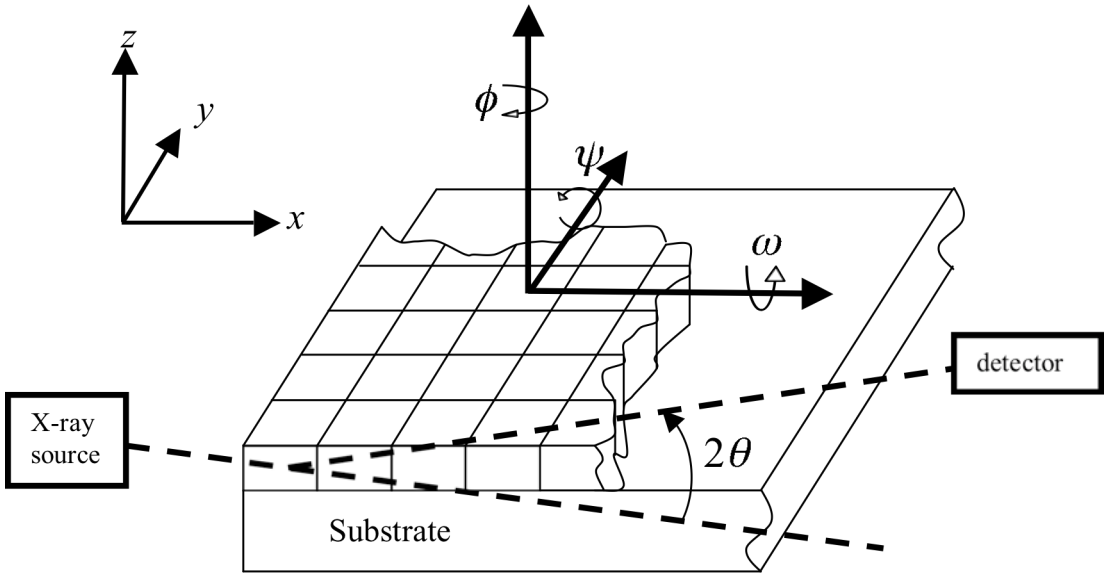

Figure 26: X-ray diffraction axes and angles

Rocking curves hold the detector constant at the Bragg angle (2θ) while the sample is rotated through ω. As the sample rotates, each subgrain in the crystal comes into orientation. Therefore, the range of ω with non-zero intensity (or above the background level, in practice) gives a measure of the range of non-oriented areas in the crystal. These areas are the result of dislocations, so the width (FWHM) is a measure of the dislocation density.

3.4.1 On-axis measurements

The in-plane twist measurement is trivial to make for a sample of known composition — a standard X-ray rocking curve measurement can be taken in the (001) direction (normal to the surface). Unfortunately, (001) is not an allowable diffraction plane. (002) is allowed, so we use (002) for quantitative data for the screw dislocation density N_{screw}.

The tilt, however, poses more problems. An XRD scan in the (100) direction (parallel to the surface) would give data on the tilt, but this is not practical in most cases since the substrate is thicker than the penetration depth of the x-ray beam. Additionally, it would be a difficult measurement to set up, since it would have to not only be aligned to a layer with a thickness on the order of μm, but it would have to remain parallel to that thin layer over the width of the entire sample, which would be difficult, if not impossible, when samples have much curvature at all. Recalling that the motivation for XRD measurements is dislocations in the sample as a result of lattice mismatch, and that dislocations also cause curvature in the sample, we find that we need an alternate method for determine the dislocation density for edge dislocations.

3.4.2 Off-axis measurements

Off-axis vectors such as (102) and (201) have components that are parallel to the plane of the sample (the desired plane for tilt measurements), so XRD measurements along these vectors will detect edge dislocations (Srikant 1997). Of course, such vectors also have components normal to the plane of the sample, so such measurements are sensitive to both edge and screw dislocations. If we take both on- and off-axis measurements, however, we can compare the data from each scan to determine the edge dislocation density.

3.4.3 Device layer characterization

As Figure 23 shows, our samples have multiple layers. Each layer nominally requires its own XRD measurement, although in practice, the diffraction points for buried layers are

still picked up when scanning thin top layers. Our samples have thicknesses ~μm, so XRD scans pick up these buried layers (AlN and sapphire).

XRD measurements of the substrate are trivial to take, and are used only periodically to check for gross deviations in substrate quality. Our sapphire substrates are bulk single-crystal Al_2O_3 wafers from commercial sources, so the dislocation density should be very small. In fact, the density is typically lower than our diffractometer can detect, so it appears as a delta function. The measurements for AlN are typically just as simple, although naturally our material quality is not good enough to be approaching the resolution of our diffractometer.

Diffraction measurements for the AlGaN device layers are more complicated, however. First, the composition of aluminum relative to gallium is unknown. We overcome this problem by taking an ω–2θ scan of the device layer. In this scanning mode, the sample is rotated around the ω axis while the diffractometer moves the detector, thereby changing θ, while maintaining the relationship

$$\omega = 2\theta. \tag{12}$$

In other words, the scan rate for θ is twice the rate for ω. In our typical samples, this scan finds peaks for both AlN and AlGaN since the AlGaN layer is so thin. To determine the relative composition, we first use Bragg's law:

$$n\lambda_X = 2d \sin\theta, \tag{13}$$

where n is the order of diffraction, d is the spacing in the diffracting material, θ is the angle between the incident beam and the diffracted point, and λ_X is the wavelength of the x-ray source (as opposed to λ, the wavelength of emitted light). These variables are illustrated below in Figure 27, the standard illustration for x-ray diffraction in a crystal structure.

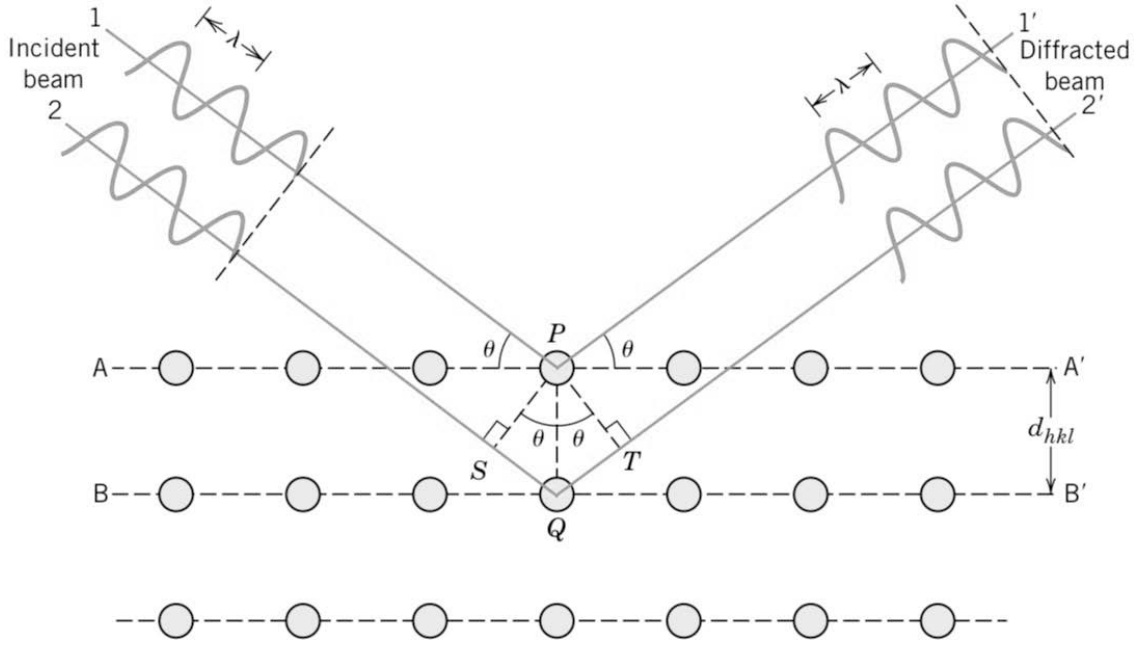

Figure 27: Diffraction of x-rays by a crystal
(Callister 2003, W-2)

When both AlN and AlGaN layers are present, as in these ω–2θ scans for composition, two diffraction conditions are simultaneously satisfied:

$$n\lambda_X = 2c_{AlN}\sin\theta_{AlN} \tag{14a}$$

$$n\lambda_X = 2c_{AlGaN}\sin\theta_{AlGaN}, \tag{14b}$$

where θ_{AlN} and θ_{AlGaN} are the central angles from the ω–2θ scan of the AlN and AlGaN peaks, respectively, and c_{AlN} and c_{AlGaN} are the c-plane lattice constants for AlN and AlGaN, respectively. Setting these equations equal to each other, we find

$$c_{AlN} \sin\theta_{AlN} = c_{AlGaN} \sin\theta_{AlGaN}. \tag{15}$$

Since AlN and AlGaN both have the same hexagonal crystal structure, the lattice constants scale linearly, according to Vegard's rule (Berger 1997, 92). Therefore,

$$c_{AlGaN} = X_{Al} \cdot c_{AlN} + X_{Ga} \cdot c_{GaN}, \tag{16}$$

where X_{Al} is the relative composition of aluminum X in the formula

$$Al_XGa_{1-X}N, \tag{17}$$

and $X_{Ga} \equiv 1 - X_{Al}$. If we substitute c_{AlGaN} from (16) into (15), we find an equation using only known variables and constants:

$$c_{AlN} \sin\theta_{AlN} = (X_{Al} \cdot c_{AlN} + X_{Ga} \cdot c_{GaN}) \cdot \sin\theta_{AlGaN}, \tag{18}$$

where the c-parameters are available in Table 3 above. Solving (18) for X_{Al} gives us the relationship necessary to determine the relative composition:

$$X_{Al} = \frac{c_{AlN} \sin(\theta_{AlN}) - c_{GaN} \sin(\theta_{AlGaN})}{(c_{AlN} - c_{GaN}) \cdot \sin(\theta_{AlGaN})}. \tag{19}$$

To find the angles of diffraction for the AlGaN layer, we must first find the lattice constants. c_{AlGaN} is given by (16) above. By the same reasoning,

$$a_{AlGaN} = X_{Al} \cdot a_{AlN} + X_{Ga} \cdot a_{GaN}. \tag{20}$$

Bragg's law, given in (13), gives the lattice spacing for a simple one-dimensional diffraction pattern. The constructive interference relationship is slightly more complicated for three-dimensional lattices. We can begin with the simplest case: a simple cubic lattice. For a such a crystal,

$$\frac{1}{d^2} = \frac{\left(h^2 + k^2 + l^2\right)}{a^2}, \tag{21}$$

where d is the spacing between diffraction points in the crystal as used in (13), h, k, and l are the components of the Miller index of the desired diffraction plane, and a is the lattice constant of the cubic crystal (Cullity 2001, 101). If we combine the previous two equations, we get the relationship

$$\sin^2\theta = \frac{{\lambda_x}^2}{4a^2}\left(h^2 + k^2 + l^2\right). \tag{22}$$

For lattices with more than one lattice parameter, this relationship becomes dependent on the lattice parameter corresponding to each Miller index. For a hexagonal crystal, the c lattice constant naturally corresponds to the l-direction. Since the structure has six-sided symmetry, however, a is linked to both the h- and k-directions. Cullity's standard *Elements of X-Ray Diffraction* gives the constructive interference relationship for a variety of crystal systems, including hexagonal crystals. The general form is similar to that for a cubic crystal:

$$\sin^2\theta = \frac{{\lambda_x}^2}{3a^2}\left(h^2 + hk + k^2\right) + \frac{{\lambda_x}^2}{4c^2}l^2. \tag{23}$$

(Cullity 2001, 303). Since the conventional diffraction angle is 2θ, we can solve the previous equation for this conventional angle, and substitute in the lattice constants for AlGaN:

$$2\theta_{AlGaN}(h,k,l) = 2\sin^{-1}\left[\left(\left(h^2 + hk + k^2\right)\left(\frac{{\lambda_X}^2}{3{a_{AlGaN}}^2}\right) + l^2\left(\frac{\lambda_X}{2c_{AlGaN}}\right)^2\right)^{1/2}\right]. \tag{24}$$

For our purposes, we will be examining only a few planes, all of which are allowable diffraction planes: (002), (102), and (201).

4 Equipment

4.1 Deposition reactor

We used a custom-built two-flow MOCVD reactor housed in the Nakamura Nitrides Laboratory at the University of California at Santa Barbara. Fundamentally, as shown in Figure 28, a substrate is mounted on a rotating susceptor, which is mounted on or near a heater, in the vicinity of a gas flow inlet. The precursors in the gas flow are trimethylgallium (TMG), trimethylaluminum (TMA), and ammonia (NH_3) in inert nitrogen or hydrogen carrier gases. The dopants (Mg in the form of magnesocene ($Mg(C_5H_5)_2 = MgCp_2$) for *p*-type, and Si in the form of silane (SiH_4) for *n*-type) also flow in this gas flow with these gases. There is another flow, the subflow, which flows the carrier gases perpendicular to the substrate. The addition of the subflow causes the reactants to continually reach the substrate. Sample rotation during growth improves uniformity. A ceramic heater using resistive heating keeps the substrate at $T \approx 1000$ °C (as measured by an *in situ* thermocouple).

Organometallic compounds in an environment free of oxygen and water undergo pyrolysis when the temperature is sufficiently high. That is, the materials chemically decompose. As the gases flow to the substrate, they adsorb on the surface. There, pyrolysis occurs, and these molecules form layers of AlN, AlGaN, or GaN epitaxially. We use a LabView-driven computer interface to automate the growth times and gas flows. Using the software, we can grow multiple layers of varying compositions in one growth run.

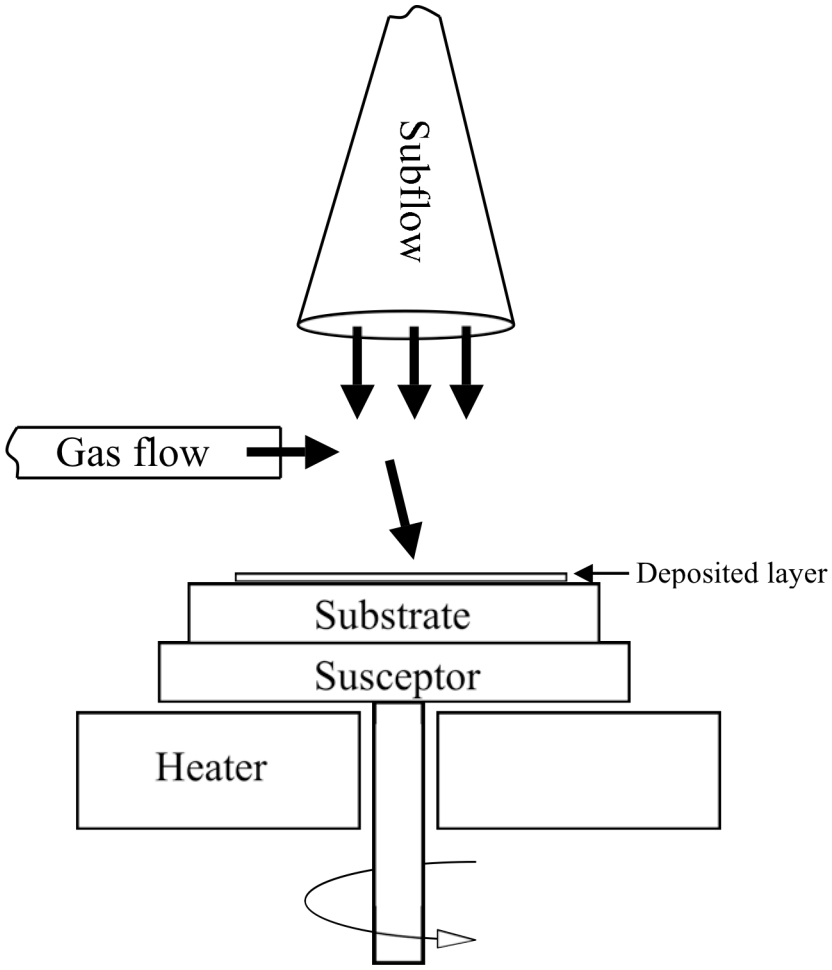

Figure 28: Two-flow MOCVD process

4.2 Characterization equipment

4.2.1 X-ray diffractometer

Two nearly identical x-ray diffractometers are housed in the Materials Research Laboratory X-Ray facility at the University of California at Santa Barbara. Both are Philips X'Pert Panalytical Materials Research Diffractometer PRO instruments which use a 18 kW Rigaku anode and a 2.2 kW Philips sealed tube source (see Figure 29 and Figure 30). The CuK_{α} source provides a wavelength of λ_X = 1.5405 Å. The resolution is

~5 arcsec for ω scans. We used Philips X'PERT Data Collector for data acquisition and Philips X'PERT Epitaxy for data processing.

The angles used in the software are consistent with Figure 26. All scans use a 0.5° slit on the detector.

Figure 29: Outside of x-ray diffractometer

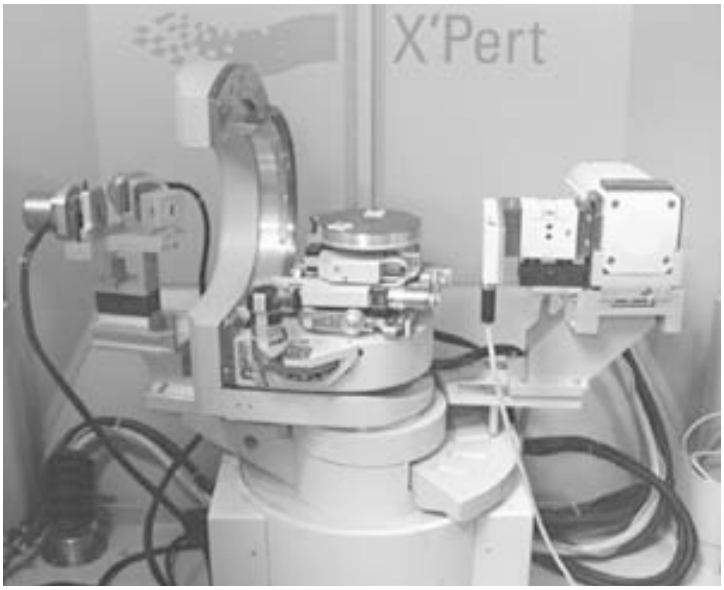

Figure 30: Inside of x-ray diffractometer

4.2.2 Optical microscope

A Nikon SD 2000 optical microscope with a Nikon digital camera attachment (see Figure 31) is housed in the Nakamura Nitrides Laboratory at the University of California at Santa Barbara. We use Nikon software for image capture, analysis, and archival.

Figure 31: Optical Microscope

4.2.3 Scanning electron microscope

The Department of Physics and Astronomy at Pomona College houses a LEO Zeiss 982 field-emission scanning electron microscope.

4.2.4 Atomic force microscope

We used Veeco/Digital Instruments Dimension 3000 and Dimension 3100 atomic force microscopes (AFM) (see Figure 32); the models are functionally equivalent. Pomona

College houses a Dimension 3100; the Department of Engineering at the University of California at Santa Barbara houses both models. We operated the AFM in tapping mode.

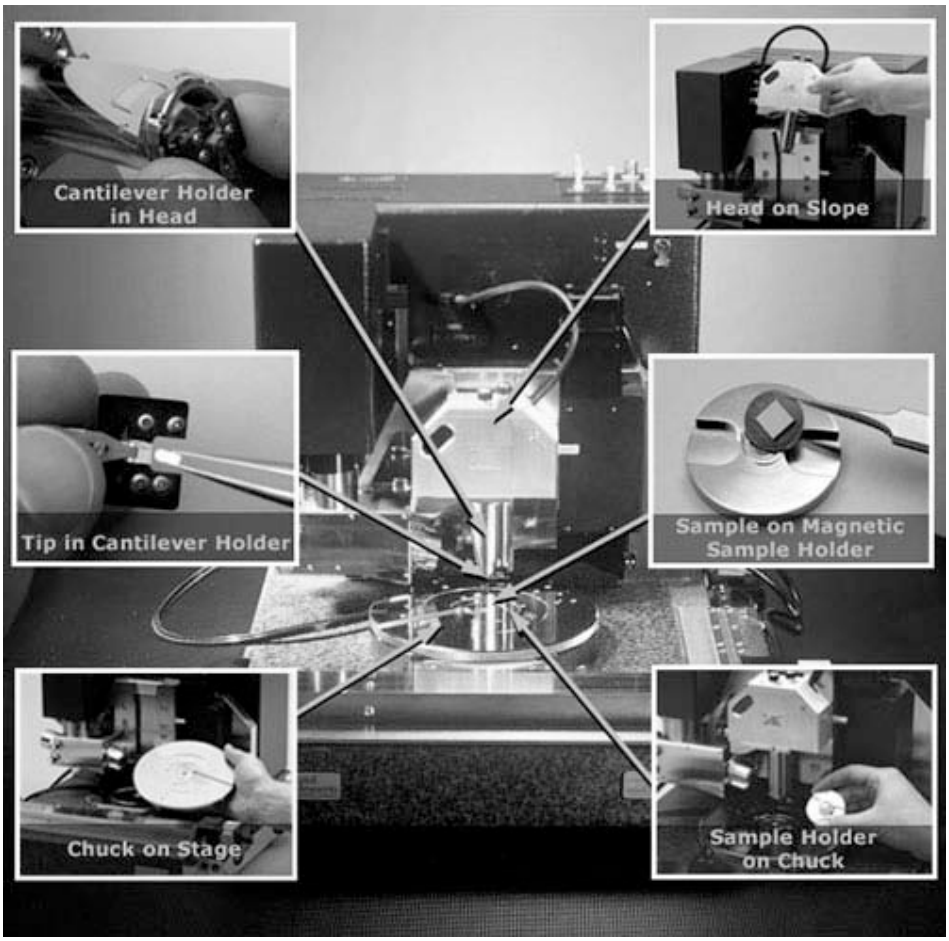

Figure 32: Atomic force microscope

5 Procedure

5.1 Deposition

The Metalorganic chemical vapor deposition (MOCVD) reactor is entirely computer-controlled. The growth steps are programmed in advance. A simple representative two-layer process is described below. Each sample is different, however, so the conditions listed below are simply a rough guide.

The sapphire substrates are shipped clean, so the only pre-reactor cleaning step is blowing the wafer off with nitrogen gas. Once loaded into the reactor, the temperature is raised to 1060 °C and the wafer is held in a hydrogen gas stream for ~10 min. At this temperature, hydrogen etches sapphire. This pre-bake or hydrogen pre-treatment step cleans and improves the surface quality and atomic step structure of sapphire through etching.

The temperature then decreases to ~700 °C and we introduce TMA and ammonia to deposit a very small layer of AlN (< 1 nm). This layer is not an atomic or continuous layer. These AlN deposits serve as nucleation points for the next step. The heater then ramps to 1100 °C – 1150 °C to deposit 0.5 μm – 1.5 μm of AlN material. We then lower the temperature to 1000 °C – 1050 °C and introduce TMG to deposit ~500 nm of AlGaN. The entire process takes place at 760 Torr in a nitrogen/hydrogen environment.

5.2 Characterization

5.2.1 X-ray diffraction

For AlN layers, the on-axis characterization process is as follows: We loaded the sample in the X'PERT diffractometer and secured it to the stage using magnets. The X'PERT software has angle presets for AlN, so we entered the desired diffraction plane (002) and the *x*, *y*, and *z* coordinates (*z* is dependent on the sample thickness and the position and size of the stage. For our diffractometer, standard stage, and standard sapphire substrate, we used $z = 9.70$ mm.). We typically used $y = 0$ and $x = 10$ mm. Since the samples are rotated during deposition, the material quality should have only a radial dependence. Therefore, *x* and *y* are essentially interchangeable. Since semiconductor devices are made from the regions on the wafer that have the best material quality, we scanned at the best quality, which is somewhere near $x = 10$ mm. We determined this by taking on- and off-axis scans at various *x*-positions, as shown in Figure 33. Note that the trend is different for on- and off-axis scans, which correspond to the different types of dislocations (note the different axes). The position around $x = 10$ is near the minimum for both types of scans.

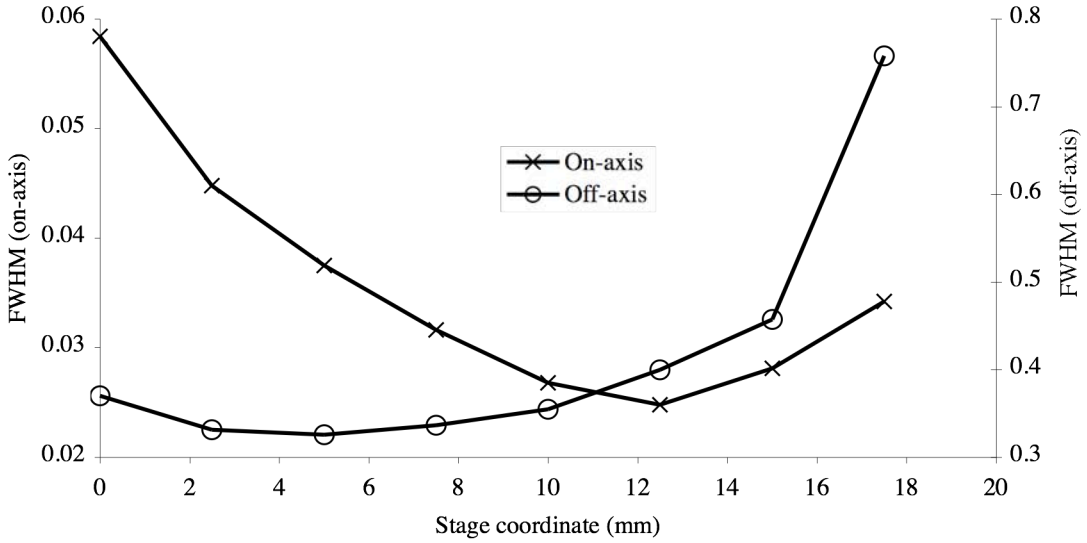

Figure 33: Radial dependence of XRD peaks

We used the X'PERT software to align the sample to the ϕ peak. Since the sample has six-fold symmetry, and since changing the ϕ angle rotates the sample about the substrate normal, there should be a ϕ peak every 30°. Therefore, since we loaded the sample with roughly the same orientation each time, we typically took initial ϕ scans of 15°. Next, centered about the software-provided ψ angle, we aligned to the ψ peak. Since the ψ peak is relatively broad, we took 12° scans. Next, we did a relatively fast ω scan to locate and center on the ω peak. Finally, we took our full-length ω scan of ~3°, depending on the peak width. The off-axis characterization process is similar. We changed the diffraction plane to (201) in the software and realigned the angles accordingly.

For AlGaN layers, the process is somewhat more complicated. The first step is to determine the relative Al and Ga composition. We determined this by first taking an ω–2θ scan. In this scan, the relationship

$$\omega = 2\theta \tag{25}$$

is maintained. In our samples, the AlGaN layer is deposited on top of the AlN buffer layer, so the AlN peak will be visible along with the AlGaN peak. If we use curve-fitting software to determine the peak angles for both peaks, we can use (19) above to determine the relative composition. Once we have the composition, we use (24) to find the theoretical diffraction angle for the AlGaN peak, since $\omega = 2\theta$. The angle ϕ should be the same for both AlN and AlGaN, since the AlGaN layer has the same orientation as the AlN layer, and ψ should also be the same. With these angles, we can take rocking curve scans of the AlGaN layer.

This technique works well for on-axis (002) scans. In practice, however, off-axis peaks are significantly broader. In fact, when I tried this procedure, the peaks were so broad compared to the separation between AlN and AlGaN peaks that it was generally not possible to obtain quantitative peak width measurements for the AlGaN layer. Of course, as outlined above, off-axis device layer peak widths are required to study the dependence of the dislocation density on the underlying layer.

There are two possible solutions — we can try to make the peaks narrower, or we can try to separate the peaks. In order to achieve the first option, material quality would, by definition, have to be improved. Unfortunately, given that significant resources have been dedicated worldwide to trying to improve the material quality, then without a breakthrough, this is the more difficult option.

The simpler option, which I hope will help the process of obtaining this high-quality material, is to separate the peaks. In a typical two-layer sample, there are only two peaks in this region (the substrate peak is not near the other peaks): AlN and AlGaN. Therefore, to separate the two peaks, we need to decrease X_{Al}. In other words, if we increase the TMG flow relative to the TMA flow, the AlGaN peak will be shifted away from the AlN peak and closer to where a GaN peak would be. This shift allows us to obtain the quantitative data we need.

One complication of increased Ga composition is that we shift away from our target wavelength, so the data is not as directly related to the device material as it would be if the samples were at the target composition. Given the years of research on GaN thin films, growing AlGaN films with low AlN composition is easier than growing films with higher AlN composition. This translates into better material quality at lower compositions, and, therefore, narrower XRD peak widths. On the other hand, growing low-AlN AlGaN layers is not entirely different from growing the layers at our target composition, so the data is indeed helpful. Moreover, if this technique results in improved film quality, and hence narrow the width of the overlapping peaks, we can start shifting the composition towards the desired composition. Put another way, we can close the gap between the peaks and retain the ability to extract the peak widths if this shift is accompanied by an improvement in the material quality.

5.2.2 Scanning electron microscopy

We conducted a brief SEM study to look at the cross-section of samples to determine the layer structure. To accomplish this, we cleaved a sample and mounted it with copper tape on a sample holder cut at a 45° angle. We then tilted the stage so we were imaging at an angle of nearly 90° (again, problems related to the motors in the stage limited tilting to a full 90°). Due to issues with charging the sample, we operated at a relatively low 3 kV.

6 Analysis

Optical microscopy indicates that the samples are not smooth, transparent films— Figure 34 and Figure 35 show cracking and deposits on the surface, respectively. In the first sample, the cracking is a result of the stress on the material. The layer has cracked along the lattice planes, which is why the lines intersect at $n \cdot 30°$ angles (n is an integer). The second sample shows metal deposits (possibly gallium) on the surface. If the rest of the material in this sample were high quality, the sample would still not make a good LED, since the deposits would block much of the emitted light. This first characterization step indicates that the samples are not the high quality material needed to produce efficient optoelectronic devices.

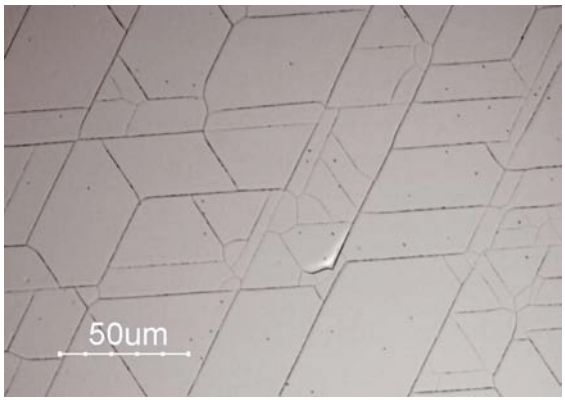

Figure 34: Cracking

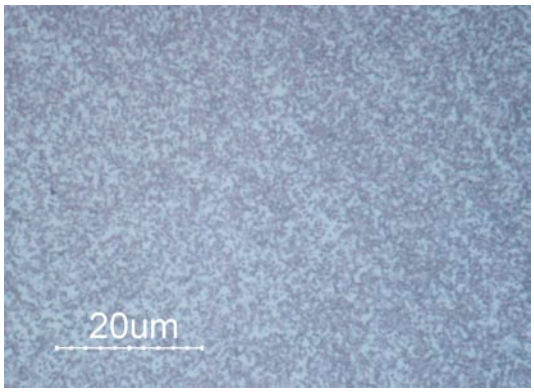

Figure 35: Deposits

Figure 36 is a cross-sectional SEM image of a standard sample (the same sample that will be used for XRD in Figure 38 below), with speculative labels for the layers of the sample. The copper tape was used to mount the sample. The bright white area around the AlGaN layer is likely caused by the material as it photoluminesces when bombarded with electrons. The detector in the SEM is a photodetector (a phosphor releases photons when

struck by electrons in conventional imaging); the photons emitted from the AlGaN layer bypass this phosphor and strike the photodetector directly.

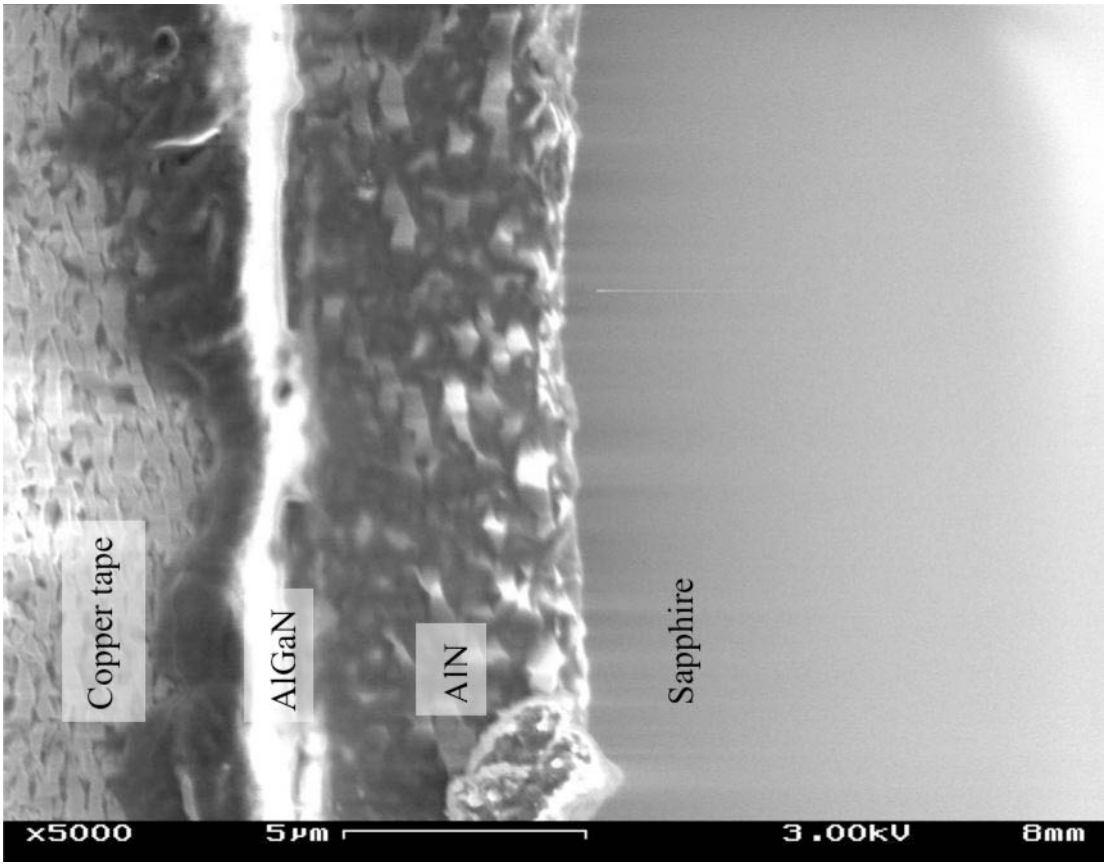

Figure 36: Cross-sectional SEM image of sample

A more quantitative investigation reveals more troubling issues. Figure 37 shows on-axis XRD data from thin films grown in May 2004 and August 2004. Recalling that the FWHM is proportional to the dislocation density, which is a measurement of material quality, we see that the film quality actually worsened over that time period. Both of these films were deposited using the standard program. The only known differences between the samples are a minor change to the reactor subflow, as well as general reactor maintenance and heater replacement. Although in fact the general film quality worsened over the period of primary research, it is fortunate that the data is still usable for

determining the relationship between dislocation densities in the template and device layers. In fact, this shift in quality helped inspire me to try the peak separation approach.

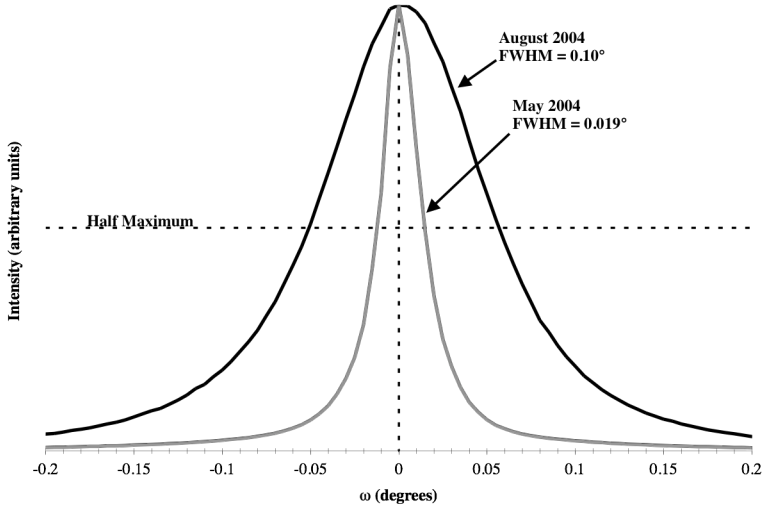

Figure 37: AlN (002) XRD scan

The initial attempts to determine edge dislocation density in the device layers using (24) failed. The XRD data for such an attempt appears in Figure 38. Since both the AlN and AlGaN peaks should be detectable, we expect two peaks. Since the peaks are separated by $\Delta\omega < 0.6°$, and since the peaks have an approximate FWHM of $\omega > 0.5°$, the peaks are not distinguishable from each other and rather appear as one broad peak with the appearance of two humps.

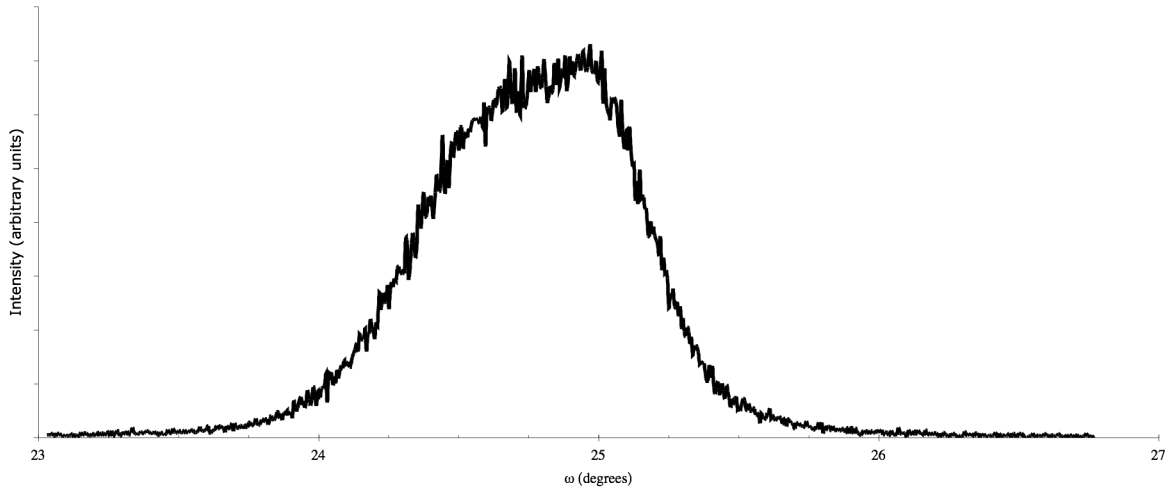

Figure 38: AlN/AlGaN (102) XRD scan, $x_{Al} \approx 0.35$

The XRD peaks for AlN, GaN, AlGaN have the following relationship:

$$\omega_{GaN} < \omega_{AlGaN} < \omega_{AlN}. \tag{26}$$

Therefore, to combat this issue, I suggested that we reduce the Al composition. Equation (26) implies that if the Al composition is reduced, and the material shifts towards greater Ga composition, that the AlGaN peak will move farther away from the AlN peak, and thus the separation $\Delta\omega$ between the AlN and AlGaN peaks will increase. We grew a new sample with a significantly lower AlN composition and repeated the off-axis AlGaN characterization process. The new XRD data appears in Figure 39. Note that the peaks are now distinguishable. We then repeated the process with intermediate compositions; the data from one such composition appears in Figure 40. (The difference in smoothness of the peaks is primarily from the difference in scanning speeds, but it is also from the difference in the intensity of the x-ray source and the material quality.) These refined peaks demonstrate the ability to measure AlGaN and AlN edge dislocation density

simultaneously. A detailed analysis of such comparative peak widths should form the basis for further study to relate the AlGaN and AlN quality (from a batch of samples with varied growth conditions), similar to the on-axis study presented below. This technique enables such a study.

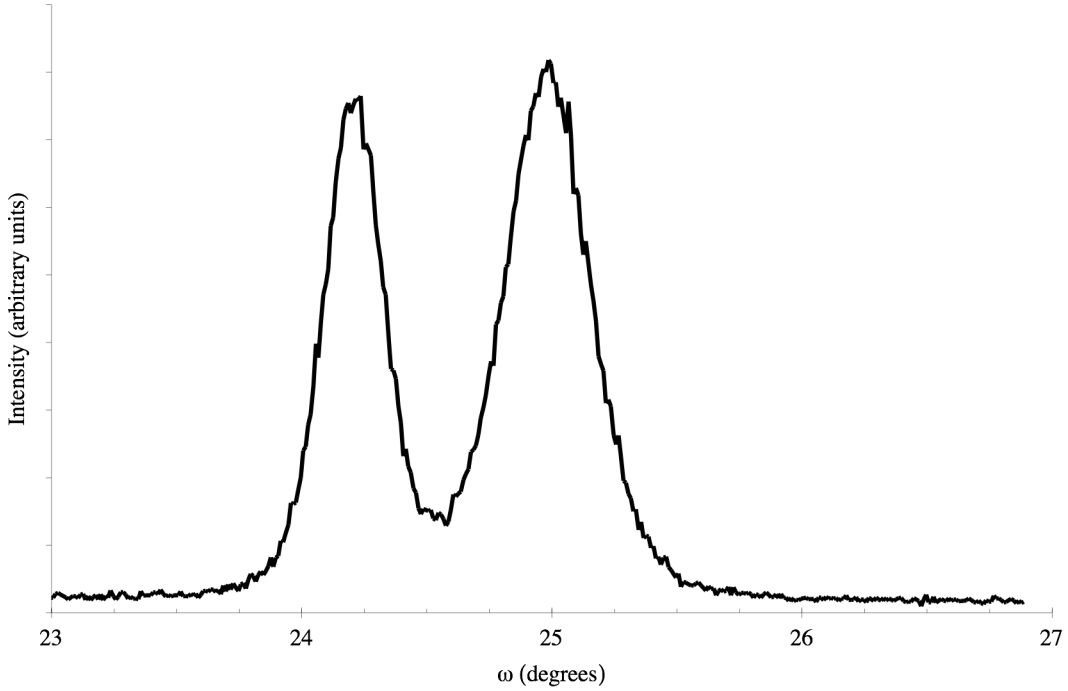

Figure 39: AlN/AlGaN (102) XRD scan, $x_{Al} \approx 0.10$

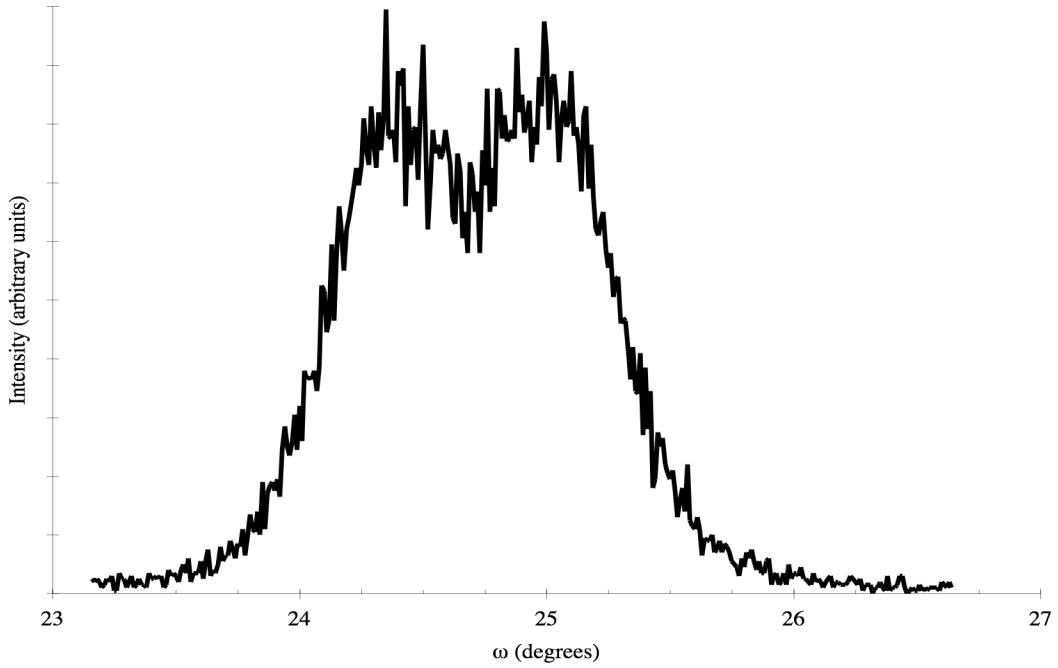

Figure 40: AlN/AlGaN (102) XRD scan, $x_{Al} \approx 0.22$

We could not always locate the AlGaN peak in reciprocal space. In practice, we could find this double-peak pattern in only roughly one third of the samples we tried. A likely cause for the difficulty in detecting this peak is the problem of simultaneously aligning all the XRD angles. For the AlN template, the computer software has a built-in preset for the AlN diffraction angles. Aligning these angles typically means making only minor adjustments (<< 1°) from the preset angles. Since there is no preset set of angles for a given composition of AlGaN, we had to make some assumptions. First, we assumed that ϕ is the same as it is for the AlN layer. Since ϕ is the orientation of the unit cell relative to the stage, and since we assume that the AlGaN layer has the same alignment as the AlN layer (and we do not move the sample), this seems to be a good assumption. Unfortunately, we could not verify this on the remaining two thirds of the samples since if even one angle is misaligned significantly, no meaningful diffraction will occur. We also assumed that ψ would be approximately the same for both AlN and AlGaN. This

might be a faulty assumption. Finally, for ω and 2θ, we used the calculated quantity from equation (24) and the relationship in equation (12). We assume, however, that the AlGaN is in a relaxed state, which may be incorrect. If the material is not in a relaxed state, Poisson's theorem indicates that the lattice constants will change. Equation (24) uses the lattice constants, so the values we use for ω and 2θ may be off because of the non-relaxed state of the material. I believe that this last explanation is the most likely candidate for the problem. The dislocations are formed by strain in the crystal, so the assumption that the material is relaxed is weak. For higher-quality material, this strain will not be as strong, so the lattice constants may not change much. This would explain why some samples do show such a diffraction pattern.

A significant amount of time was dedicated to merely being able to extract quantitative data from the off-axis AlGaN XRD patterns. Unfortunately, this meant there was no time left to perform a complete study of the relationship between the AlN and AlGaN layer material qualities with all other variables held constant. The samples presented above were grown not only with different compositions, but under different reactor conditions.

Fortunately, the on-axis peaks were attainable for all four samples used in the next study. In a preliminary experiment, we deposited AlGaN films using the same reactor conditions on AlN templates with significantly different on-axis material quality. The correlation of the results, as shown below in Figure 41 and Table 4, suggest that the AlGaN material quality does depend on the underlying AlN template layer quality, as indicated by the FWHM of the on-axis XRD. However, even with this limited data set,

we see that a nearly 60% reduction in the AlN dislocation density corresponds to a reduction of only about 20% in the AlGaN dislocation density.

Table 4: On-axis AlN/AlGaN comparison

AlN 002 XRD FWHM (°)	AlGaN 002 XRD FWHM (°)
0.0759	0.1564
0.0759	0.1732
0.1823	0.1893
0.1823	0.1944

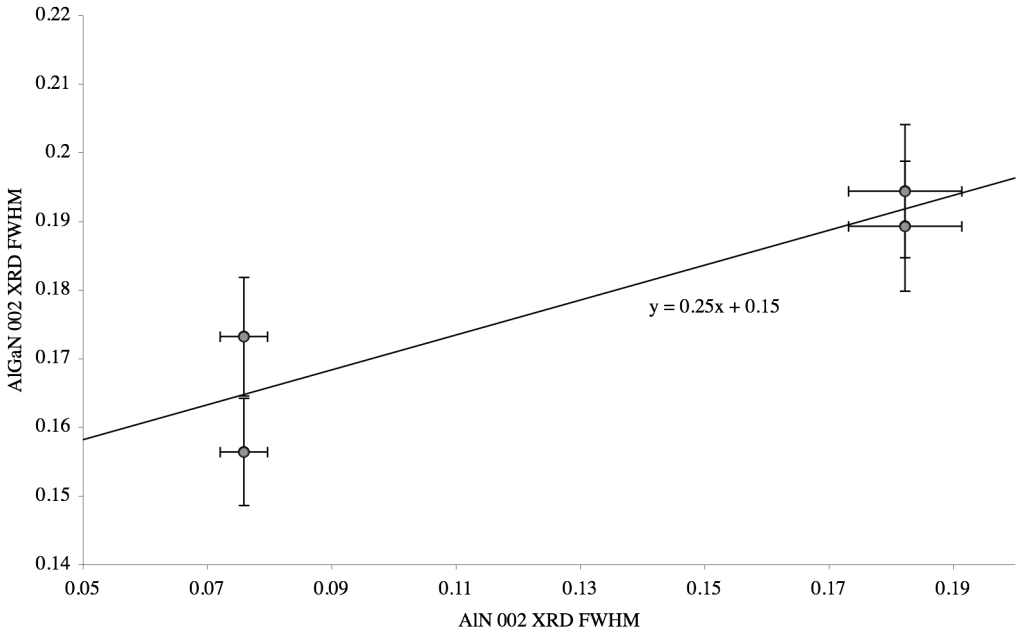

Figure 41: On-axis XRD comparison

In fact, since the off-axis experiment was successful, there is now a method to quantitatively characterize the edge dislocation density, and methods for optimizing the AlGaN layer directly, independent of the AlN layer, should be investigated. Further

investigations of this type were limited by the reactor, which suffered a heater failure shortly after the samples used in Figure 41 were grown.

Before this project, the primary quantitative characterization performed on deep-UV LED structures was XRD of the AlN layer, which is really an indirect measurement. In fact, theory tells us that dislocations can terminate at material interfaces, so it is possible that this indirect measurement was of relatively little value. The methods I propose here provide a means for characterizing the device layer of the samples. I also started the process of determining the relationship between the material quality of the AlN and AlGaN layers. The next step is to make use of these new techniques and, aided by a better understanding of more samples, determine this relationship and use the appropriate optimization techniques to improve the device layer quality.

7 Conclusions

The next step in the expansion of the spectrum covered by LEDs and laser diodes is into the deep-UV region. A likely material system for this region is AlGaN on sapphire due to its large direct bandgap. Since AlGaN is an immature material system, there is still significant work to be done to optimize the material. Good characterization techniques are critical to the optimization process. Previously, there was no good method to quickly characterize AlGaN material quality — TEM is time consuming and labor-intensive, but known XRD methods failed to reveal measurements for off-axis device layer quality. Accordingly, optimization techniques focused on optimizing the AlN buffer layer that is commonly used to lessen the effects of the large lattice mismatch between AlGaN and sapphire. This is an indirect measurement of AlGaN quality at best. At worst, it is a completely unrelated measurement.

We grew AlGaN layers on AlN buffer layers on sapphire substrates using metalorganic chemical vapor deposition. I successfully created a method to quickly characterize the AlGaN material quality, using an initial compositional x-ray diffraction scan and a series of equations that give angles that can be entered into a diffractometer. This technique worked for roughly one third of the samples. Unfortunately, reactor complications prevented us from attaining a large data set to relate AlN quality to AlGaN quality. An initial on-axis data set suggests that the relationship is weak — a 60% decrease in dislocation density in the AlN layer corresponded to only a 20% reduction in the dislocation density of the AlGaN layer.

8 References

"Light-emitting diode," *Wikipedia*, (2005). Available: http://en.wikipedia.org/wiki/LED.

"Blu-Ray Disc," *Wikipedia*, (2005). Available: http://en.wikipedia.org/wiki/Blu-ray_Disc.

"Ultraviolet," *Wikipedia*, (2005). Available: http://en.wikipedia.org/wiki/UV.

"History of LED Technology," *Marktech Optoelectronics Engineering Services*, Available: http://www.marktechopto.com/engineering/history.cfm.

Adivarahan, V., S. Wu, J. P. Zhang, A. Chitnis, M. Shatalov, V. Mandavilli, R. Gaska, and M. A. Khan. "High-efficiency 269 nm emission deep ultraviolet light-emitting diodes," *Appl.Phys.Lett.* **84**, 4762 (2004).

Berger, Lev I., *Semiconductor Materials*. (CRC: Boca Raton, FL, 1997).

Buerger, Martin J., *Contemporary Crystallography*. (McGraw-Hill: n.p., 1970).

Callister, William D., *Materials Science and Engineering: An Introduction*. 6 ed. (Wiley: New York, 2002).

Carrano, LTC John C. "Semiconductor Ultraviolet Optical Sources (SUVOS)," *Defense Advanced Research Projects Agency*, Department of Defense, Available: http://www.darpa.mil/mto/suvos/.

Cullity, B. D. and S. R. Stock, *Elements of X-Ray Diffraction*. 3 ed. (Prentice Hall: Upper Saddle River, NJ, 2001).

Duley, W. W., *UV Lasers: Effects and Applications in Materials Science*. (Cambridge UP: Cambridge, 1996).

Elert, Glenn. "Color," *Physics Hypertextbook*, (2005). Available: http://hypertextbook.com/physics/waves/color.

Evans, R. C., *An Introduction to Crystal Chemistry*. (Cambridge UP: Cambridge, 1966).

Fairchild, Mark D., *Color Appearnce Models*. 2 ed. (Wiley: West Sussex, England, 2005).

Fischer, A. J., A. A. Allerman, M. H. Crawford, K. H. A. Bogart, S. R. Lee, R. J. Kaplar, W. W. Chow, S. R. Kurtz, K. W. Fullmer, and J. J. Figiel. "Room-temperature direct current operation of 290 nm light-emitting diodes with milliwatt power levels," *Appl.Phys.Lett*. **84**, 3394 (2004).

Fraser, D. A., *The Physics of Semi-Conductor Devices*. (Clarendon: Oxford, 1977).

Garni, B., Jian Ma, N. Perkins, Jutong Liu, T. F. Kuech, and M. G. Lagally. "Scanning tunneling microscopy and tunneling luminescence of the surface of GaN films grown by vapor phase epitaxy," *Appl.Phys.Lett*. **68**, 1380 (1996).

Hanlon, A., P. M. Pattison, J. F. Kaeding, R. Sharma, P. Fini, and S. Nakamura. “292 nm AlGaN single-quantum well light emitting diodes grown on transparent AlN base,” *Jpn. J. Appl. Phys. 2, Lett. (Japan)* **42**, L628 (2003).

Hansen, P. J., Y. E. Strausser, A. N. Erickson, E. J. Tarsa, P. Kozodoy, E. G. Brazel, J. P. Ibbetson, U. Mishra, V. Narayanamurti, S. P. DenBaars, and J. S. Speck. “Scanning capacitance microscopy imaging of threading dislocations in GaN films grown on (0001) sapphire by metalorganic chemical vapor deposition,” *Appl.Phys.Lett*. **72**, 2247 (1998).

Haskell, Ben. "Structure of Nonpolar Gallium Nitride Films Grown by Hydride Vapor Phase Epitaxy." Dissertation from University of California at Santa Barbara. (2005: Santa Barbara, CA).

Heying, B., X. H. Wu, A. S. Keller, Y. Li, D. Kapolnek, B. P. Keller, S. P. DenBaars, and J. S. Speck. “Role of threading dislocation structure on the X-ray diffraction peak widths in epitaxial GaN films,” *Appl.Phys.Lett*. **68**, 643 (1996).

Hull, Derek, *Introduction to Dislocations*. (Pergamon Press: London, 1965).

Kapolnek, D., X. H. Wu, B. Heying, S. Keller, B. P. Keller, S. P. DenBaars, and J. S. Speck. “Structural evolution in epitaxial metalorganic chemical vapor deposition grown GaN films on sapphire,” *Appl.Phys.Lett.* **67**, 1541 (1995).

Koechner, Walter, *Solid-State Laser Engineering*. 5 ed. (Springer: Berlin, 1999).

Koleske, D. D., A. J. Fischer, A. A. Allerman, C. C. Mitchell, K. C. Cross, S. R. Kurtz, J. J. Figiel, K. W. Fullmer, and W. G. Breiland. “Improved brightness of 380 nm GaN light emitting diodes through intentional delay of the nucleation island coalescence,” *Appl.Phys.Lett.* **81**, 1940 (2002).

Luidia. “Background Images,” Luidia UK, Available: http://www.luidiauk.com/education/background%20images.htm.

Nakamura, Shuji, Gerhard Fasol and Stephen J. Pearton, *The Blue Laser Diode: The Complete Story*. 2 ed. (Springer-Verlag: Berlin, 2000).

Nichia. “NSPW500BS,” *Specifications for Nichia White LED*.

Parish, Giacinta. "Growth and Characterization of Aluminum Gallium Nitride / Gallium Nitride Ultraviolet Detectors." Dissertation from University of California at Santa Barbara. (2001: Santa Barbara, CA).

Rosner, S. J., E. C. Carr, M. J. Ludowise, G. Girolami, and H. I. Erikson. “Correlation of cathodoluminescence inhomogeneity with microstructural defects in epitaxial GaN grown by metalorganic chemical-vapor deposition,” *Appl.Phys.Lett.* **70**, 420 (1997).

Srikant, V., J. S. Speck, and D. R. Clarke. “Mosaic structure in epitaxial thin films having large lattice mismatch,” *J.Appl.Phys.* **82**, 4286 (1997).

Suryanarayana, C. and M. Grant Norton, *X-Ray Diffraction: A Practical Approach*. (Plenum: New York, 1998).

Wang, T., Y. H. Liu, Y. B. Lee, J. P. Ao, J. Bai, and S. Sakai. "1 mW AlInGaN-based ultraviolet light-emitting diode with an emission wavelength of 348 nm grown on sapphire substrate," *Appl.Phys.Lett.* **81**, 2508 (2002).

Weimann, N. G., L. F. Eastman, D. Doppalapudi, H. M. Ng, and T. D. Moustakas. "Scattering of electrons at threading dislocations in GaN," *J.Appl.Phys.* **83**, 3656 (1998).

9 Acknowledgements

This work made use of MRL Central Facilities supported by the MRSEC Program of the National Science Foundation under award No. DMR00-80034. Our sapphire substrates were provided by Namiki Precision Jewel Co. Additional support came from the SUVOS program run by DARPA, as well as Mitsubishi Chemical. My support came from the UCSB Materials Research Lab Research Intern in Science and Engineering program as well as the National Nanotechnology Infrastructure Network Research Experience for Undergraduates program.

I would personally like to thank many individuals that contributed to this work, beginning with the faculty at Pomona. I'd of course like to thank Dr. Richard Mawhorter for venturing outside of his comfort zone for this project, as well as years of good advice and support. Thanks to Dr. Charles Taylor for bridging the gap across College Avenue and for giving me a different perspective on the problem. Thanks to Dr. David Tanenbaum for his generous offer to use his equipment and his expertise even when he's enjoying his year in snowy Ithaca. Thanks to Dr. Thomas Moore for his expertise in technical drawing — without this help, readers might be scratching their heads over some confusing amateur drawings. Thanks also to the support staff like Dave Haley, who helped out with the SEM, Connie Wilson for administrative support, and Dr. Alfred Kwok and Dr. Alma Zook for years of helpful advice.

Next, I'd like to thank the Nakamura group at UCSB. First, thanks to Dr. Shuji Nakamura for opening his lab to me, as well as his expertise and the offer to return a second

summer. Thanks to Ed Letts for his initial guidance as well as his help in returning. Thanks to John Kaeding (JFK) for taking time out of his busy research schedule to help answer all my questions, as well as his willingness to take the research in new directions. Thanks also to the UCSB support staff (Paul Fini and Brian Carralejo) for their useful advice and constant amusement.

Finally, I'd like to thank the people who helped me get to where I am. Marisa Muscari deserves a big thanks for all of her support, as well as her willingness to relocate to Millikan basement for a semester. Thanks to my two previous roommates Michael Neuss and Ryan Montoya for putting up with my late-night physics work, and to Han Ban who kept me going with physics. My whole family deserves thanks, as well. My siblings Kendra, Greg, and Brent, all pushed me to follow my physics dreams and helped me the whole way. My mother was always willing to listen to my physics lessons, and my father would stay up all night talking shop with me. They taught me that sometimes you learn more in failure than in success. While this project was certainly not a failure, the challenges along the way taught me more than I could have imagined. Thank you to everyone involved.